Collapse Dynamics of Confined Liquid Films

Graduation committee:

Chairman:
Prof. dr. ir. B. Poelsema (University of Twente, TNW)

Promotor:
Prof. dr. F. Mugele (University of Twente, TNW)

Assistant Promotor:
Prof. dr. S. Herminghaus (MPI f. Dynamik u. Selbstorganisation, Göttingen)

Committee members:
Prof. dr. W. Briels (University of Twente, TNW)
Prof. dr. ing. D.H.A. Blank (University of Twente, TNW)
Dr. J.C.T. Eijkel (University of Twente, EWI)

The research described in this dissertation was carried out in the Department of Applied Physics at the University of Ulm, Germany. Financial support was provided by the German Science Foundation in the priority program "Wetting and Structure Formation at Interfaces".
This dissertation was publicly defended on the 30^{th} of June 2005 at the University of Twente in the Complex Fluids Group.

Collapse Dynamics of Confined Liquid Films

Thomas Becker

ISBN 90-365-2210-2

Printed by F56 Druck & Copy, 89073 Ulm (Germany)

COLLAPSE DYNAMICS OF CONFINED LIQUID FILMS

DISSERTATION

to obtain
the doctor's degree at the University of Twente,
on the authority of the rector magnificus,
prof.dr. W.H.M. Zijm,
on account of the decision of the graduation committee,
to be publicly defended
on Thursday June 30$^{\text{th}}$ 2005 at 13.15

by

Thomas Becker

born on July 9$^{\text{th}}$ 1974

in Hannover, Germany

The dissertation is approved by the promotor Prof. Dr. Frieder Mugele and the assistant promotor Prof. Dr. Stephan Herminghaus.

Abstract

Liquids in a confined geometry have attracted much interest in science and technology in recent years. Confined liquid films with a thickness in the range of a few molecular diameters exhibit different mechanical properties than in the bulk. In this work a newly designed surface forces apparatus with two-dimensional imaging capability is presented. Due to the unprecedented sensitivity of the two-dimensional imaging technique the dynamics of the layer by layer thinning of a confined liquid film can be investigated in great detail.
Different expulsion scenarios depending on the substrate elasticity and the approach rates are presented. Applying slow approach rates to both stiff and soft substrates results in similar dynamics of the expulsion processes. A comparison of the dynamics with a simple hydrodynamic model shows good agreement. In the case of particularly thin substrates with fast approach rates the formation of small trapped liquid droplets and their subsequent squeeze-out was observed. Fast approaches on thick substrates resulted in a mixed drainage scenario.
While it is generally accepted that the viscosity of confined liquids increases with decreasing thickness, the order of magnitude is highly debated. The viscosity of a model lubricant (OMCTS) is measured as a function of the thickness of the confined film and found to increase by a factor of ten with

decreasing film thickness from 6 to 2 layers. This is in contrast to results reported by others where an increase of several orders of magnitude was observed. Importantly, in our experiments, a method to improve the standard preparation procedure was used. In order to describe the increase in the effective friction observed in our work a new hydrodynamic model is presented. In terms of this model it is shown that the sliding friction of liquid layers on top of the solid substrates is approximately 35 times higher than the mutual friction between adjacent liquid layers. The latter is independent of film thickness and in close agreement with the bulk viscosity. The mentioned variations in mechanical properties of thin liquid films compared to the bulk properties arise from structural changes. Making use of recent advances in synchrotron radiation sources and beam shaping techniques allows the investigation of the in-plane structure of confined liquids with x-ray scattering experiments. Preliminary x-ray scattering data from thin liquid crystalline films (8CB) are shown and the domain structure of the liquid crystal and the anchoring of the liquid crystal with respect to the mica lattice is discussed.

Contents

1. Introduction

1.1. Perspectives on the collapse dynamics of liquid films

Tribology is the science and technology of interacting surfaces in relative motion. Tribology plays a critical role in a large number of very diverse technological areas. For example, tribological studies aid in optimising the lifespan of mechanical components in the automotive industry and help refine polishing processes in the semiconductor industry [1]. In recent times, a detailed knowledge of tribology at the nanometer scale has become a requirement of many industries. Nanotribology as a field is concerned with experimental and theoretical investigations of processes in the atomic and molecular regime that occur during friction, adhesion, wear, and thin-film lubrication at sliding surfaces. The latter area is the focus of this dissertation.

The study of thin liquid films between solid substrates has become an intense area of research over the last few decades (see, for example [1–19]). This attention is the result not only of their importance in technological applications but also due to their ubiquitous existence in Nature [1]. For example, in the human body reduced friction in our hip and knee joints is obtained with thin liquid lubricant layers and in plants ultrathin capillaries enable the distribution of water [1]. In technological applications, such as microelectro-

mechanical systems (MEMS), the drive towards smaller and smaller devices means that the thinness of the relevant lubricant layers is approaching molecular dimensions [1]. The collapse or expulsion of these ultrathin lubricant layers from the sliding surfaces results in excessive wear and ultimately device failure. Thus, understanding the mechanisms that govern the stability of these ultrathin lubricant layers are of crucial importance.

To date, a complete understanding of the fundamental effects of confinement and solid-liquid interaction on the structural and mechanical properties of thin liquid films does not exist and a number of papers deal with this topic (for example, [1–20] and references therein). The most accurate techniques for experimental studies of this subject require well defined geometries with planar substrates. Such a geometry is realised in a surface forces apparatus (SFA) [3]. In this instrument, two atomically smooth surfaces are mounted onto cylindrical curved sample holders and brought into a well-defined position (Figure 1(a)). As shown in Figure 1(b), the two surfaces form a slit pore with parallel walls at the apices. The liquid can thus be confined to a gap of adjustable width. When confined to atomic dimensions between opposing surfaces it has been shown that simple liquids adopt a layer structure parallel to the surface (Figure 1(c)) and display extremely unusual properties in comparison to their bulk behaviour. For instance, if two substrates are pressed together the film thickness decreases continuously as long as the behaviour of the bulk liquid is followed. In contrast, a stepwise decrease in film thickness is observed when the film thickness is reduced to a few molecular diameters [3–5].

In the present contribution, a modified SFA [6, 7] is constructed that allows a two-dimensional analysis of the dynamic processes in molecularly thin films in order to study in detail the expulsion dynamics of molecularly thin lubricant films upon increasing normal pressure. Furthermore,

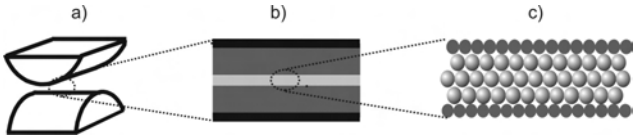

Figure 1.1: Sample geometry in a surface forces apparatus on different length scales. (a) Crossed cylinder configuration. (b) Parallel plate geometry with mirrors (black), atomically flat substrate (dark gray) and the confined liquid (light gray). (c) The layered structure of a molecularly thin film (dark gray: atomically flat substrate; light gray: confined liquid molecules.)

the optical SFA set-up is combined with recent advances in synchrotron radiation sources and beam shaping techniques that enable more detailed investigations of the structure of the molecules within single layers.

1.2. Thesis outline

The outline of this thesis is the following: after this brief introductory chapter some basic properties of confined liquid films are surveyed. Included here is a detailed description of the theoretical models used to describe expulsion processes. Original work then begins in Chapter 3 with the development of a unique two-dimensional imaging SFA. The novel technique developed to prepare ultra-clean surfaces is also discussed in this chapter. The experimental procedures and data analysis techniques utilised in the remainder of this thesis are also presented here. In Chapter 4 the optical part of the experimental set-up is described in detail. The results of the measurements made with the two-dimensional SFA are presented. A unique capability of the instrumentation devel-

oped is that direct observations of the expulsion dynamics of single liquid layers can now be made. This is a significant result and in Chapter 5 different expulsion scenarios are studied in detail. The dynamics of the experimentally determined expulsion processes are then compared with theoretical models. A detailed analysis of some of the experimental results in Chapter 5 show an anomaly when compared to theory and form the basis of the experimental work discussed in Chapter 6. In this chapter detailed investigations of the structure of the molecules within single layers is made possible with x-ray scattering measurements. Finally, Chapter 7 ends the dissertation by means of a conclusion. Future experiments are also briefly proposed and discussed.

2. Theory

This chapter provides an overview of the theoretical concepts underlying the experiments performed on thin liquid films under confinement. In the beginning, the behaviour of liquids confined between solid walls is discussed. Different experimental techniques to investigate the confined liquids are briefly presented. The experimental observation of the expulsion of single liquid layers is a highlight of the work in this thesis and thus a significant portion of this theory chapter is dedicated to understanding a simple hydrodynamic model [1, 2] which will ultimately aid in the detailed analysis of the dynamical processes observed.

2.1. Confined liquids

The liquid state of matter is characterised by a random positional arrangement of the molecules combined with a high mobility. Solid walls confining the liquid to a finite volume impose constraints primarily on the arrangement of the molecules. In the vicinity of walls, however, constraints on the positional order also hinder place exchanges and thereby tend to reduce the molecular mobility. In Nature, liquids are frequently confined in random porous media, such as rocks. Technological confinement geometries are frequently more two-dimensional, e.g. in lubrication applications. In both cases, the combination of the geometric confinement and the

interaction of the solid substrates with the liquid affect the behaviour of the liquid and can lead to significantly different properties than observed in the bulk phase.

2.1.1. The breakdown of continuum theories

The structure of the solid state depends essentially on the minimum of the potential energy of the interaction between the particles, such as the Lennard Jones interaction for simple non-polar liquids. In the liquid state, the average separation between adjacent molecules is similar to the solid state. However, random thermal motion allows for frequent site exchanges. No coherent long range order exists. In Figure 2.1, we plot the probability of finding a second molecule at a distance r from a reference molecule in the origin for a bulk liquid. This distribution is isotropic. The deep minimum between zero and the particle diameter σ is due to the hard short range repulsion arising essentially from geometric overlap. The first maximum corresponds to a shell of nearest neighbours surrounding (on average) the reference molecule. After a next minimum, which is due the repulsive interaction with the molecules in the first shell, there is another shell of, now, second-nearest neighbours. Due to the random molecular motion discussed above, the amplitude of the second shell is much smaller than the first one, and the same applies even more for the third shell. Eventually, the probability drops to the value corresponding to the bulk liquid density.
Let us now consider the forces acting between two solid surfaces across a liquid-filled gap. At large distances, the forces can be described by continuum theories such as the DLVO theory [21, 22]. This theory describes the electromagnetic interactions between particles or solute molecules in a liquid medium, i.e. mainly van der Waals and electrostatic forces. At sufficiently small separations the van der Waals attraction

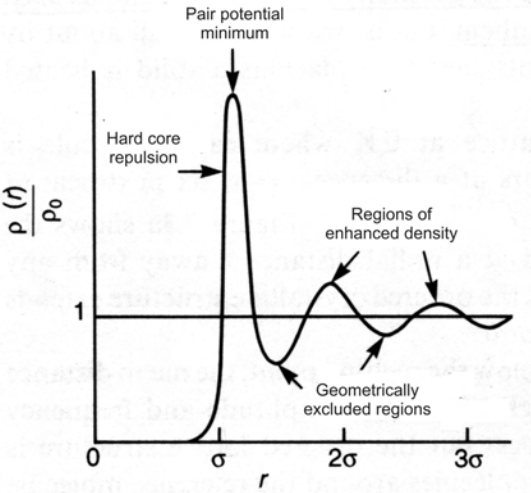

Figure 2.1: Using x-ray and neutron scattering experiments the liquid density profile of bulk liquids is obtainable (taken from [3]).

always exceeds the double-layer repulsion since it diverges as a power law whereas the double-layer interaction remains finite or increases comparatively slowly giving rise to an overall attractive force. Experimentally, the DLVO theory is known to fail for liquid films with a thickness comparable to the molecular dimensions. In this range, the forces between two (sufficiently, i.e. atomically, smooth) surfaces in simple liquids are observed to vary between attraction and repulsion with a periodicity matching some dimension of the confined liquid molecules [5,8,23]. In this regime the molecular nature of the intervening liquid must be taken into account. The

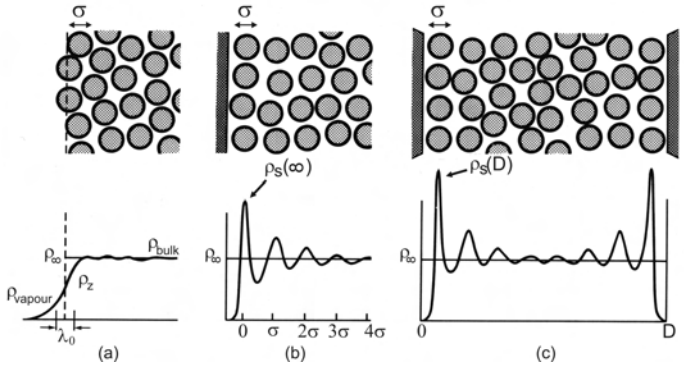

Figure 2.2: (a) The liquid density profile at a vapour-liquid interface. (b) The liquid density profile at an isolated solid-liquid interface. (c) Liquid density profile in a confined system with two solid-liquid interfaces separated by a distance D. (Taken from [3]).

exact separation at which these forces become oscillatory depends on the properties of the liquid as well as that of the surfaces. These deviations from the predictions of continuum theory are referred to as solvation effects and the oscillatory forces as solvation forces [4]. Oscillatory forces and large periodic density variations between two smooth solid surfaces approaching each other in a simple liquid were first predicted in the late 1970s [24–26]. The origin of the oscillatory forces is closely related to the density oscillations described above. Theoretical studies and particularly computer simulations indicate that while liquid density oscillations are not expected to occur at a liquid-vapour (Figure 2.2(a)) or liquid-liquid interface the situation is very different at a solid-liquid interface (Figure 2.2(b)). Computer modelling of fluids at solid surfaces show that the oscillatory solvation force originates from the ordering of molecules in layers when the liquid is con-

fined by the surfaces (i.e. "molecular layering") [27]. This organisation into discrete layers in the liquid is not necessarily a result of some complicated substrate-liquid interaction but can result simply from the presence of a hard wall barrier. The short-range repulsive potential forces the liquid molecules to stay at a minimum distance. Even for a single ideal planar wall, the same effect as described above for the bulk liquid gives rise to a one-dimensional density oscillation perpendicular to the surface (see Figure 2.2b). The density modulation perpendicular to the surface typically decays to zero within a few molecular layers and the value of the bulk density is then observed [25, 26]. In a confined system the density modulations caused by each interface interfere with each other (Figure 2.2(c)). The overlap of density oscillations gives rise to the oscillatory solvation forces.

2.1.2. Experimental probes of confined liquids

The properties of a confined liquid can be investigated using different techniques. For random porous media with large amounts of confined liquid, techniques such as calorimetry, dielectric spectroscopy [28], nuclear magnetic resonance [29,30], as well as scattering techniques revealed important information. The focus of the present thesis, however, is in on well-defined pore geometries, which have mainly been studied using the surface force apparatus (SFA) and the atomic force microscope (AFM) (see for example [8–12, 31–34]). The SFA was developed in the late 1960s [35, 36] to measure forces between surfaces in air and is now commonly used to study both the static and dynamic properties of liquids confined between two molecularly smooth surfaces. Typically two solids with atomically flat surfaces are immersed in a liquid and the force between the two surfaces is measured as a function of the distance. As with AFMs and most other force-mea-

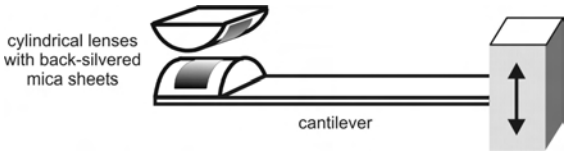

Figure 2.3: A schematic diagram illustrating a typical experimental SFA set-up.

suring devices, the SFA determines forces from the deflection of a spring. The displacement is measured using optical, electrical, capacitive or strain-gauge techniques. The most common technique is optical multiple beam interferometry, which allows for a resolution of approximately 0.1 nm. Thus the SFA allows the measurement of the normal and lateral forces between surfaces in liquids at separations that are precisely controlled and measured in the Angstrom range. The force measurement itself is closely linked to the thickness measurements: The base of the force-measuring spring (see 2.3) is moved by a calibrated translation device. Any deviation between the relative displacement of the two surfaces (as determined from the interferometry measurement) and the displacement of the translation device is due a bending of the spring induced by forces acting between the two surfaces. The force resolution thus achieved is typically in the range of micro Newtons. A schematic diagram of the experimental arrangement of a SFA is shown in Figure 2.3. Typically, the surfaces have a radius of curvature on the order of 1cm. The introduction of the atomic force microscope in the mid 1980s provided a new method for measuring ultra-small forces between a probe tip (that can be as small as one atom or larger than 1 μm) and a surface [37]. A useful way to consider the AFM is the "small ball on a weak sping model" illustrated in Figure 2.4(a) [38]. This model

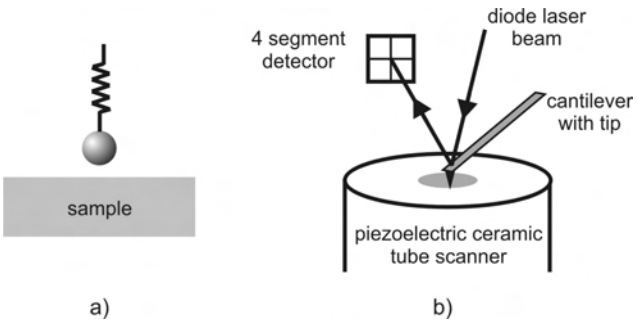

Figure 2.4: (a) The "small ball on a weak spring model" useful for understanding the key features of an AFM. (b) A schematic diagram of a typical AFM set-up.

emphasises the central features of the AFM as a mechanical sensor for probing interaction forces. In contrast to the SFA the measured quantity is not the separation of the two interacting surfaces but the interaction force. This is achieved by measuring the deflection of the spring - usually by detecting the deflection of a laser beam that is reflected from the deflected cantilever spring (2.4(b) [38]). As in the case of SFA, the mechanical system can be represented by a weak mechanical spring with one of the interacting surfaces attached to it. In practice, the spring consists of a small cantilever made from Si or SiN with a length and width on the order 100 μm and 10 μm, respectively. The surface attached to this cantilever is typically a sharp tip etched from the same material with a radius of curvature at the apex between 10 and 100 nm. A detailed account of the implementation of AFM can be found elsewhere [39] and a typical set-up is shown in Figure 2.4(b) [38]. In the context of force measurements in liquids, the sharp tip is frequently replaced by a colloidal sphere with a much larger radius (e.g. 10 μm) [32, 34, 40–42].

One problem that arises in these measurements is that the actual separation of the two surfaces has to be inferred indirectly from the force curve. Compared to SFA measurements, this can lead to a substantial uncertainty.

2.2. Dynamics of expulsion processes

In this section we present models for the squeeze out of liquid films in three different regimes. We begin with a purely hydrodynamic description assuming infinitely stiff walls. Next we take into account the finite elasticity of the substrates which leads to elastohydrodynamic effects. Finally, we analyse the squeeze out dynamics of molecularly thin films, which are affected by the discrete layer structure. This regime was described previously by Persson *et al.* [1,2], whose work we are going to summarise briefly.

2.2.1. Hydrodynamic drainage

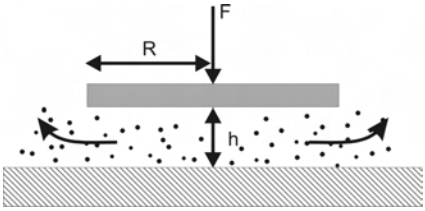

Figure 2.5: A rigid circular disk is pushed against a flat rigid surface. An incompressible liquid in between can be described using the Navier-Stokes equation. Taken from [17].

Consider the situation shown in Figure 2.5, where a flat cir-

cular disk is pushed with a force F towards a flat surface in a fluid. Both surfaces are assumed to be rigid and the liquid behaves as a Newtonian fluid. For an incompressible liquid the velocity field $\vec{v}(\vec{x},t)$ and the pressure field $P(\vec{x},t)$ are obtained by solving the continuity equation and the Navier-Stokes equation:

$$\nabla\vec{v} = 0 \tag{2.1}$$

$$\frac{\partial\vec{v}}{\partial t} + \vec{v}\cdot\nabla\vec{v} = -\frac{1}{\rho}\nabla P + \nu\nabla^2\vec{v}. \tag{2.2}$$

Here, ρ is the mass density and $\nu = \eta/\rho$ is the kinematic viscosity. In general one has $Re \ll 1$ for squeezing, where Re is the Reynolds number, which is given by $Re = v_0 h/\nu$. Here, v_0 is a characteristic velocity and h is a characteristic separation between the solid walls. Thus the liquid flow can be regarded as laminar. Under these conditions Equation 2.2 reduces to the Stokes equation:

$$\nabla P = \eta\nabla^2\vec{v} \tag{2.3}$$

In classical hydrodynamics this equation is solved using the no-slip boundary condition. With this boundary condition the pressure distribution for the situation shown in Figure 2.5 is given by:

$$P = P_{\text{ext}} - \frac{3\eta\dot{h}}{h^3}(R^2 - r^2), \tag{2.4}$$

where $\dot{h} = \mathrm{d}h/\mathrm{d}t$ is the approach velocity of the disk to the plate and P_{ext} is the external applied pressure. With these definitions, the approach velocity during the squeezing process is negative, $\dot{h} < 0$. As a consequence, the pressure P in the film is larger than the external pressure for $r < R$ and separating the plates ($\dot{h} > 0$) may lead to cavitation. Using $\sigma_0 = F/\pi R^2$ the thickness $h(t)$ of the liquid layer at the time t is determined by

$$\frac{1}{h^2(t)} - \frac{1}{h^2(0)} = \frac{4t\sigma_0}{3\eta R^2}. \tag{2.5}$$

Thus, in this purely hydrodynamic description the film thickness decreases continuously with time. Similar calculations have also been performed for a sphere plane geometry, which has attracted a lot of interest in recent years [34, 43–45]. Both, AFM and SFA experiments revealed that the classical no-slip boundary condition is frequently violated between the molecular and the submicrometre range [43, 46].

2.2.2. Elastohydrodynamics

For a more realistic description, the surfaces usually cannot be regarded as perfectly rigid. The pressure distribution in the liquid during the approach deforms the surfaces elastically and this deformation then influences the flow field in the liquid. Consider for example a soft sphere that is pushed against a plate. In the case without liquid the contact region

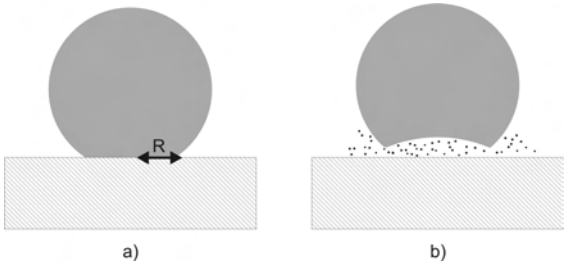

Figure 2.6: a) Pushing a soft sphere against a rigid plate results in a flat and circular contact region. b) The sphere is elastically deformed when it is pushed against the plate in a surrounding fluid. Taken from [17].

will be circular and flat with radius R. If P_0 is the the average external pressure, the pressure distribution within the

contact area is given by the Hertz solution (see for e.g. [3]):

$$P = P_0 \frac{3}{2} \sqrt{1 - \left(\frac{r}{R}\right)^2} \tag{2.6}$$

Pushing the sphere against the plate in a liquid, the pressure in the center of the contact region is larger by a factor of $4/3$ compared to Equation 2.6), thus

$$P = 2P_0 \sqrt{1 - \left(\frac{r}{R}\right)^2}. \tag{2.7}$$

For a detailed description both the elastic and the hydrodynamic equations have to be solved simultaneously. However, qualitatively the difference between the hydrodynamic (Equation 2.7) and the elastic pressure gives rise to an elastic deformation of the sphere. This may lead to trapping of liquid droplets (see Figure 2.6b)). The stability and squeeze out behaviour of liquid films in this regime have been investigated by [47, 48].

2.2.3. Layer by layer squeeze out

In order to describe the dynamics of single collapsing layers, this section provides a summary of the findings of B.N.J Persson *et al.* [1, 2, 17]. An understanding of these results forms a solid ground work for the understanding of the results presented in the latter chapters of this dissertation.
The Persson Tosatti (PT) model considers liquid films with a layered structure. Experimentally, this layered structure has been observed for atomically smooth substrates at a separation of a few molecular diameters [3–5, 8, 11–14, 49, 50]. Applying an external pressure on the confining walls results in a step-wise decrease of the film thickness.
To describe the dynamics of these expulsion processes we

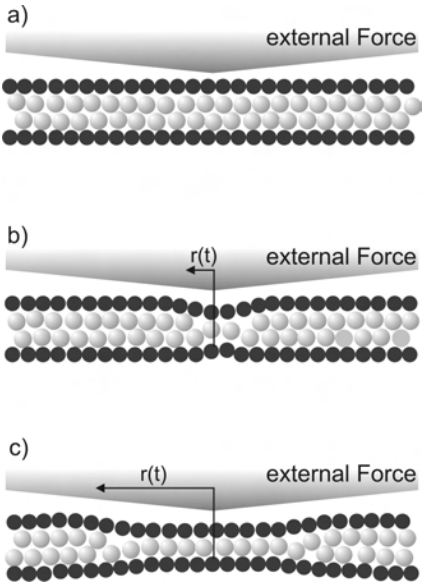

Figure 2.7: Schematics of the expulsion process $n = 2 \rightarrow 1$.

now consider the situation in Figure 2.7, where the expulsion process $n = 2 \rightarrow 1$ is schematically shown. In terms of the PT-model the squeeze out of liquid layers is described as a two stage process. For a transition from thickness $n \rightarrow (n-1)$ first a small area of reduced film thickness nucleates. Once a critical nucleus is formed it spreads and grows over the contact area.
Due to a thermal fluctuation a small circular hole nucleates in the two-dimensional liquid layer. After the nucleus has formed the system can gain energy by elastic relaxation of the substrates. The energy required to create this hole can

be written as

$$U(R) = 2\pi R\Gamma + \pi R^2 p_0 - \alpha R^3, \tag{2.8}$$

where R denotes the radius of the island with reduced film thickness $(n-1)$. The first term describes the free energy related to the unsaturated bonds of the molecules at the periphery of the hole. Here, Γ represents the line tension. The second term in Equation 2.8 denotes the change in interface free energy. The pressure p_0 is usually called the spreading pressure [51–53]. The last term gives the elastic relaxation energy, with $\alpha \sim P^2/E$ (where E is the elastic modulus of the confining walls). The probability of the nucleation of a hole is given by the Boltzmann distribution and thus is temperature dependent:

$$w = w_0 e^{-\frac{U(R_c)}{k_B T}} \tag{2.9}$$

where in this equation R_c is the critical radius for which $U(r)$ is maximal. Typically the critical radius $R_c \approx 10-15$ Å and is thus too small to be visualised optically. The value of the nucleation barrier $U(R_c)$ is accessible via measuring the average force required to induce a layer expulsion process depending on the load rate. For these kinds of experiments atomic force microscopy has been used by H.J. Butt *et al.* [34,44,45]. After the formation of a hole the area with reduced film thickness (n-1) spreads quickly across the whole contact region. Assuming the film to be in a liquid like state and to be incompressible, the basic equations to describe the motion of the lubrication film are the continuity equation (Equation 2.1) and the Navier-Stokes equation (Equation 2.2). For a two dimensional mass density ρ_{2D} the latter can be written as

$$\frac{\partial \vec{v}}{\partial t} + \vec{v}\nabla\vec{v} = -\frac{1}{\rho_{2D}}\nabla p + \nu\nabla^2\vec{v} - \overline{\eta}\vec{v}. \tag{2.10}$$

Here the last term is a "drag force", which was introduced to describe the friction between the liquid layer and the sub-

strate. It can be shown on dimensional grounds, that both the non-linear term on the left hand side and the viscosity term on the right hand side can be neglected [2], which leads to

$$\frac{\partial \vec{v}}{\partial t} = -\frac{1}{\rho_{2D}} \nabla p - \overline{\eta} \vec{v}. \tag{2.11}$$

Let us assume a circular shaped contact region with radius R and a circular nucleus at the centre of the contact area. Neglecting boundary instability effects [18,54,55] the boundary line between the area with thickness n and (n-1) remains circular with a growing radius $r(t)$. For $p_1(r)$ being the pressure at the moving boundary line and for p_0 being the spreading pressure at the edge of the contact area ($r = R$) one obtains [2]

$$\frac{dA(t)}{dt} ln \left[\frac{A(t)}{A_0} \right] = -\frac{4\pi(p_1 - p_0)}{\rho_{2D}\overline{\eta}} \tag{2.12}$$

where $A(t) = \pi r^2$ denotes the area of film thickness (n-1) and $A_0 = \pi R^2$ is the contact area. If $P(r)$ is the normal stress acting in the contact area (under the assumption of circular symmetry) and a is the thickness of one liquid layer, it can be found that [2,56]

$$p_1 = p_0 + P(r)a. \tag{2.13}$$

For a constant normal stress P_0 Equation 2.13 becomes position independent and after integration one obtains

$$\frac{A(t)}{A_0(t)} \left(ln \left[\frac{A(t)}{A_0} \right] - 1 \right) = -\frac{t}{\tau} \tag{2.14}$$

where τ denotes the time of the complete expulsion process of one liquid layer. An analytical solution can also be obtained for a Hertzian pressure profile (see Section 5.1.1) [57]. Setting $A(\tau) = A_0$ results in

$$\tau = \frac{\rho_{2D}\overline{\eta}A_0}{4\pi(p_1 - p_0)}. \tag{2.15}$$

In order to estimate the friction coefficient $\overline{\eta}$ one can use Equation 2.13 including a constant normal stress P_0

$$\overline{\eta} = \frac{4\pi\tau P_0 a}{\rho_{2D} A_0}. \tag{2.16}$$

For the case that the nucleation does not occur in the centre of the contact region but slightly off-centred, the assumptions made above are no longer valid. Thus one has to turn to numerical simulations. Here, it is assumed that the pressure in the contact area is constant and the non-linear and the viscosity term in Equation 2.10 are neglected. Furthermore, by assuming that the change of the velocity field is very slow, one can also neglect the time derivative and Equation 2.10 can be written in a simplified form

$$\nabla p + \rho_{2D}\overline{\eta}\vec{v} = 0. \tag{2.17}$$

It follows that

$$\vec{v} = \nabla\phi \qquad \text{with} \qquad \phi = -\frac{p}{\rho_{2D}\overline{\eta}} \tag{2.18}$$

and using the continuity equation (Equation 2.1) it finally yields a convenient starting point for numerical treatment [56, 58]

$$\nabla^2\phi = 0. \tag{2.19}$$

The difference from Equation 2.14 is the absence of the explicit time dependence. This quasistatic approximation assumes that the flow field rearranges much faster than the motion of the boundary line. As it can be seen the velocity potential ϕ can be regarded as an electrostatic potential. Mathematically now the problem is similar to finding an electrostatic potential bewteen two conducting cylinders at different potentials given by $\phi_0 = -p_0/\rho_{2D}\overline{\eta}$ and $\phi_1 = -p_1/\rho_{2D}\overline{\eta}$.

3. Experimental system and procedures

One of the main tasks of the work in this thesis involved the setting-up of a two-dimensional imaging surface forces apparatus (SFA). This consisted of both setting up all the devices necessary to perform the experiments and also of writing the programs necessary to control the experiment and analyse the data. One of the first SFA was developed by J.N. Israelachvili [59]. With their instrumentation, forces were measured as a function of surface separation. The latter was determined using multiple beam interferometry, which is also the key for the two-dimensional imaging technique in our SFA. The difference between the conventional set-up and our two-dimensional imaging SFA derives from the illumination of the samples. To obtain a two-dimensional transmission image we have used monochromatic light with a wavelength on the wing of a transmission peak to illuminate the contact region of the surfaces.
In the beginning of this chapter the experimental set-up and all the components used for the measurements on thin liquid films will be presented. Since the sample preparation is of critical importance for successful experiments, the steps involved will be described in detail in this chapter. To date, the preparation procedure and the related cleanliness has been a controversial issue. Here, we have introduced an additional preparation step into the standard procedure in order to obtain ultra-clean surfaces. In addition to the discussion of the

equipment set-up and the preparation of the samples, the experimental procedures and the analysis techniques of the experimental data will also be presented.

3.1. Experimental set-up

Figure 3.1 shows a schematic sketch of the experimental set-up of the two-dimensional imaging SFA. The key components of

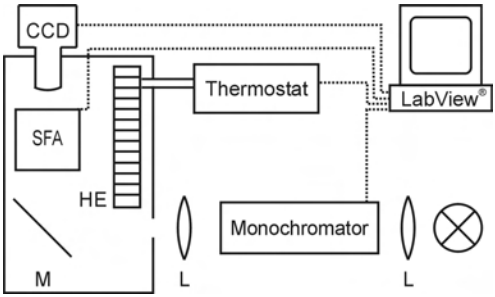

Figure 3.1: Schematic diagram of the two-dimensional imaging experimental set-up (M: mirror, L: lenses, HE: heat exchanger).

the experiment are a white light source, a grating monochromator, a CCD-camera and the SFA-cell which is contained within a temperature-controlled box. To reduce vibrations, all the components except the lamp and its power supply are mounted on an optical table. The complete set-up is controlled via custom written LabView® programs. In the following sections all components will be described in detail. A list of the equipment used, including the relevant technical specifications, is provided in Appendix A.

3.1.1. Optics

A special feature of the experimental technique used in this thesis for the investigation of thin liquid films under confinement is the capability of two-dimensional imaging with a thickness resolution better than 1 nm. Recording two-dimensional images of the contact area in transmission allows a detailed investigation of the dynamics of the expulsion of single molecular layers. From the dynamics it is then possible to determine the friction coefficient of these single molecular layers with unprecedented sensitivity.
The sample system in SFA experiments consists of several optical layers shown schematically in Figure 3.2. In the contact

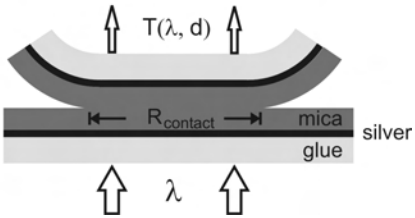

Figure 3.2: A schematic diagram of a typical SFA multi-layer system.

area the mica substrates are flattened elastically (see also Figure 2.3). The outer layers of this multi-layer system are silver layers with a thickness of 40-45 nm. These silver layers act as mirrors with a transmission of approximately 4% and a reflectance of approximately 95% [60]. The mirrors are evaporated on the backside of thin sheets of mica. In the case of the measurements with a liquid, a liquid film is confined between the two mica layers. Thus, the sample geometry in SFA experiments is equivalent to a Fabry-Perot interferometer and multiple beam interferometry techniques can be used

to determine the thickness of the confined film. In the following, the mathematical principles used to describe optical properties of our multi-layer system will be explained [61]. Consider a plane wave of monochromatic light, propagating in a medium with refractive index n_1 incident on a transparent plate with refractive index n_2 at the angle θ. At the top surface of the plate this wave is divided into a reflected wave and into a wave transmitted into the plate. The latter wave is incident at an angle θ' on the bottom surface and is subsequently divided into a transmitted wave leaving the plate and into a reflected wave, which propagates back into the plate. This process of division of the wave continues as indicated in Figure 3.3. These multiple reflections result in

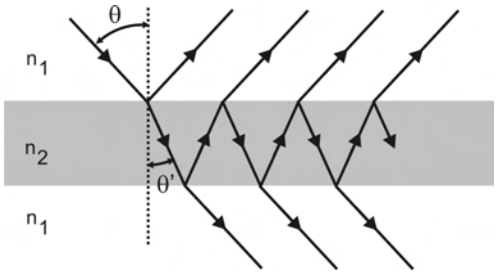

Figure 3.3: Reflection of a plane wave in a plane parallel plate [61].

a series of interfering beams with diminishing amplitudes on each side of the plate [61]. The reflection and transmission coefficients of a beam of light propagating from a medium 1 into medium 2 are given by:

$$r_{12} = \frac{n_1 - n_2}{n_1 + n_2} \tag{3.1}$$

$$t_{12} = \frac{2n_1}{n_1 + n_2} = 1 + r_{12} \tag{3.2}$$

respectively. In the case of a medium with a complex refractive index, such as for the silver mirrors used in the SFA experiments, the reflected light wave will experience a phase change ϕ, where

$$\phi_{12} = \arg(r_{12}). \tag{3.3}$$

Increasing the number of optical layers to a system consisting of a medium with refractive index n_b and thickness d_b confined between two media with refractive indices n_a and n_c, the equations for the reflection and transmission coefficients of the system become more complex:

$$r_{ac} = \frac{r_{ab} + r_{bc}e^{i(2kd_bn_b)}}{1 + r_{ab}r_{bc}e^{i(2kd_bn_b)}} \tag{3.4}$$

$$t_{ac} = \frac{t_{ab}t_{bc}e^{i(kd_bn_b)}}{1 + r_{ab}r_{bc}e^{i(2kd_bn_b)}} \tag{3.5}$$

where k is the wavenumber in these equations. Obviously, as the optical system is extended to include more and more layers the analytical formulae become increasingly complex. In order to calculate the wavelength dependent transmission through the optical multi-layer systems used in the SFA experiments (Figure 3.2), the so-called matrix method was applied [61, 62]. The advantage of this method is that optical layers can be removed or added to the system with relative ease. The principle of this method is that each optical layer in the system can be described with a characteristic matrix M_i, which contains all its optical properties and relates the fields at the upper and the lower boundary. The transmission and reflection of a system consisting of N layers can then be calculated using the characteristic transfer matrix $\mathbf{M}$:

$$\begin{pmatrix} E_{\mathrm{I}} \\ H_{\mathrm{I}} \end{pmatrix} = \mathbf{M} \begin{pmatrix} E_{\mathrm{II}} \\ H_{\mathrm{II}} \end{pmatrix} \tag{3.6}$$

The characteristic matrix of the whole system is given by:

$$\mathbf{M} = \prod_{i=1}^{N} \mathbf{M}_i. \tag{3.7}$$

Consider a linearly polarised wave impinging on a system as shown in Figure 3.4. At the upper surface of the plate one has:

$$E_{\mathrm{I}} = E_{i\mathrm{I}} + E_{r\mathrm{I}} = E_{t\mathrm{I}} + E'_{r\mathrm{II}} \tag{3.8}$$

and

$$H_{\mathrm{I}} = \sqrt{\frac{\epsilon_0}{\mu_0}}(E_{i\mathrm{I}} - E_{r\mathrm{I}})n_0 \cos\theta_{i\mathrm{I}} = \sqrt{\frac{\epsilon_0}{\mu_0}}(E_{t\mathrm{I}} - E'_{r\mathrm{II}})n_1 \cos\theta_{i\mathrm{II}}. \tag{3.9}$$

The electric and the magnetic field in nonmagnetic media are related through the index of refraction and the unit propagation vector:

$$\mathbf{H} = \sqrt{\frac{\epsilon_0}{\mu_0}} n\mathbf{k} \times \mathbf{E}. \tag{3.10}$$

At the lower boundary the fields are given by:

$$E_{\mathrm{II}} = E_{i\mathrm{II}} + E_{r\mathrm{II}} = E_{t\mathrm{II}} \tag{3.11}$$

and

$$H_{\mathrm{II}} = \sqrt{\frac{\epsilon_0}{\mu_0}}(E_{i\mathrm{II}} - E_{r\mathrm{II}})n_1 \cos\theta_{i\mathrm{II}} = \sqrt{\frac{\epsilon_0}{\mu_0}} E_{t\mathrm{II}} n_s \cos\theta_{t\mathrm{II}}. \tag{3.12}$$

A wave travelling through the medium with n_1 undergoes a shift in-phase given by $k_0(2n_1 d\cos\theta_{i\mathrm{II}})$ and will be written as kh_0 in the following. We thus obtain

$$E_{i\mathrm{II}} = E_{t\mathrm{I}} e^{-ik_0 h} \quad \text{and} \quad E_{r\mathrm{II}} = E'_{r\mathrm{II}} e^{+ik_0 h}. \tag{3.13}$$

Equations 3.11 and 3.12 can now be written as:

$$E_{\mathrm{II}} = E_{t\mathrm{I}} e^{-ik_0 h} + E'_{r\mathrm{II}} e^{+ik_0 h} \tag{3.14}$$

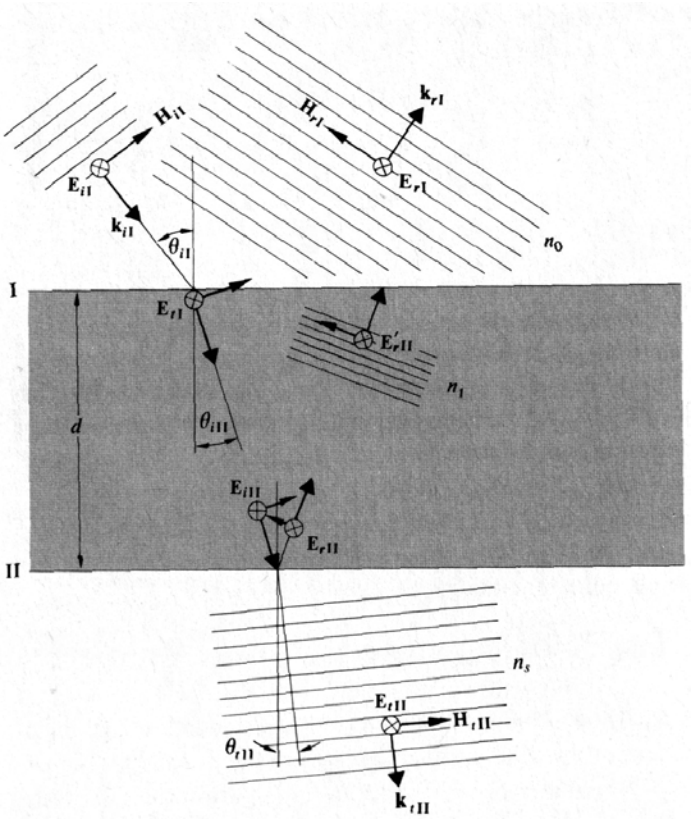

Figure 3.4: Magnetic and electric fields at the boundaries of a thin dielectric film (taken from [62]).

and

$$H_{II} = (E_{t\mathrm{I}} e^{-ik_0 h} + E'_{r\mathrm{II}} e^{+ik_0 h}) \sqrt{\frac{\epsilon_0}{\mu_0}} n_1 \cos\theta_{i\mathrm{II}}. \qquad (3.15)$$

Solving these last two equations and substituting into Equations 3.8 and 3.9 yields:

$$E_{\mathrm{I}} = E_{\mathrm{II}} \cos k_0 h \quad + \quad H_{\mathrm{II}} (i \sin k_0 h)/p_{\mathrm{I}} \qquad (3.16)$$

$$H_{\mathrm{II}} = E_{\mathrm{II}} p_{\mathrm{I}} i \sin k_0 h \quad + \quad H_{\mathrm{II}} \cos k_0 h \qquad (3.17)$$

where p_{I} is given by

$$p_{\mathrm{I}} = \sqrt{\frac{\epsilon_0}{\mu_0}} \cos\theta_{i\mathrm{II}}. \qquad (3.18)$$

Similar results are obtained for a wave with **E** being in the plane of incidence, but then p_{I} has to be written as:

$$p_{\mathrm{I}} = \sqrt{\frac{\epsilon_0}{\mu_0}} / \cos\theta_{i\mathrm{II}}. \qquad (3.19)$$

Thus, the matrix in Equation 3.6 is given by:

$$\mathbf{M}_j(d) = \begin{bmatrix} \cos(k_0 h) & \frac{i}{p} \sin(k_0 h) \\ ip \sin(k_0 h) & \cos(k_0 h). \end{bmatrix} \qquad (3.20)$$

Using Equation 3.7 it is now possible to calculate a characteristic matrix for any multi-layer system. The reflection and the transmission coefficients of the multi-layer system can be obtained from its total characteristic matrix as follows:

$$r = \frac{(m_{11} + m_{12} p_B) p_A - (m_{21} + m_{22} p_B)}{(m_{11} + m_{12} p_B) p_A + (m_{21} + m_{22} p_B)} \qquad (3.21)$$

$$t = \frac{2 p_A}{(m_{11} + m_{12} p_B) p_A + (m_{21} + m_{22} p_B)} \qquad (3.22)$$

with

$$p_A = \sqrt{\frac{\epsilon_A}{\mu_A}} \cos\theta_A \qquad \text{and} \qquad p_B = \sqrt{\frac{\epsilon_B}{\mu_B}} \cos\theta_B \qquad (3.23)$$

characterising the outer layers A and B of the system. Including the mathematical operations described into custom-written MatLab programs, the transmission through the layer systems used in our experiments can be calculated easily. For the calculations of the transmission presented in this work, the relatively thick glue layers were assumed to be the outer medium (with $n_{\mathrm{glue}} = 1.5$). The complex refractive index for the evaporated silver mirrors was taken from [63].
One technique to determine the thickness of a medium confined between the two mirrors is the so-called FECO-technique (**F**ringes of **E**qual **C**hromatic **O**rder). Here, the samples are illuminated from below with white light and the transmitted wavelengths are analysed using a spectrograph. Knowing the refractive index of the medium between the Ag mirrors the thickness can be calculated from the measured transmission peaks. The procedures for these calculations will be explained in more detail in Section 3.2.4. In contrast to the FECO-technique, we illuminate our sample system from below with monochromatic light generated by a monochromator. Adjusting the monochromator to a wavelength at which the system shows transmission then allows two-dimensional images to be taken from the contact area. The white light source used in the experiments is a bright 300 W xenon arc lamp with an intensity spectrum shown in Figure 3.5. Using a set of silver mirrors and lenses the parallel white light is focussed to the entrance slit of a 1/8 m grating monochromator. The refraction grating used features 1200 lines/mm. The monochromator is equipped with entrance and exit slits which can be adjusted to six fixed values between 0.05 and 3.16 mm in width. The light at the exit of monochromator has a triangular shaped intensity distribution $\Delta\lambda$ around the central wavelength λ_0. The width of the wavelength distribution depends on the width of the slits and can be varied in the range of $\Delta\lambda = 0.28..10.00$ nm. Using a lens, the divergent light at the exit of the

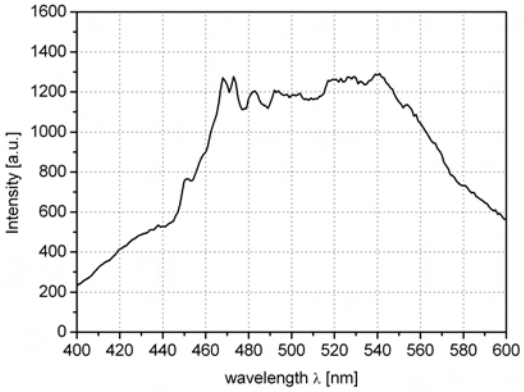

Figure 3.5: Intensity spectrum of the Xe-arc-lamp recorded with the CCD-camera used.

monochromator is made parallel and fed with another mirror through the sample system mounted in the SFA-cell. In order to determine the thickness of the single layers from the wavelength of the transmitted light it is of crucial importance to know the wavelength of the monochromatic light as accurately as possible. Thus a Hg-Ar-lamp is used to calibrate the monochromator. The lines at λ_1=435.833 nm and λ_2=546.074 nm from the Hg-Ar-lamp spectra were used for the calibration. A digital CCD-camera with 1360×1024 pixels and 12 bit resolution is used to record the transmitted light. The maximum frame rate at full frame acquisition is 10 frames/s. Operating the camera in a 2×2 binning mode the maximum frame rate can be increased to 20 frames/s. To collect the light transmitted through the samples the camera is equipped with long distance microscope objectives (5× magnification: NA=0.13, WD=22.5 mm; 20× magnification:

NA=0.35, WD=20.5 mm). This results in a maximum lateral resolution of 0.98 pixel μm^{-1} for the 5× magnification and 4.17 pixel μm^{-1} for 20× magnification which is beyond the optical resolution.

3.1.2. The SFA-cell

The central feature of all the experiments performed in this thesis are custom designed experimental cells. Two unique cells have been developed, each taking into account the specific requirements of the experiments being performed. SFA1 was designed exclusively for use in the optical experiments concerning the collapsing dynamics of single liquid layers. SFA2 was designed specifically with structure analysing x-ray scattering experiments in mind. A description of the features of both cells follows in the remainder of this section.

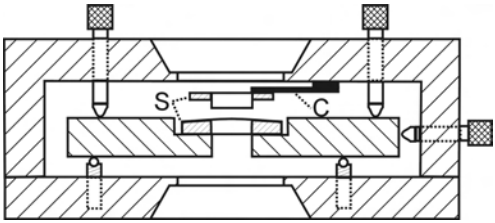

Figure 3.6: Schematic sketch of SFA1 (S: sample holder, C: cantilever)

A schematic sketch of SFA1 is shown in Figure 3.6. The chamber itself is manufactured from stainless steel and has a diameter of 120 mm and a height of 45 mm. In contrast to the conventional design, we tried to reduce the mechanical loop between the two mica surfaces by attaching the upper sample directly to the top wall of the cell via a leaf spring. The spring

constant of this cantilever is $k_{cantilever} = (110 \pm 10)$ N/m. The lower sample support is mounted rigidly onto the centre plate also made of stainless steel. The centre plate is pressed against three micrometer screws via three steel springs. The spring constant of these springs ($k_{spring} = 1.215$ kN/m) is much higher than that of the cantilever. The micrometer screws are used for the coarse approach of the two surfaces. Furthermore, it is possible to align the surfaces with these screws. For an additional lateral translation of the centre plate, two further micrometer screws are provided in the side wall of the cell. The centre plate is pressed against these screws again with two springs. The fine approach of the surfaces is controlled via magnetic forces. For this purpose the upper sample support is equipped with strong permanent magnets (NdFeB). A magnetic coil placed on top of the cell generates a magnetic field acting on the permanent magnets. Thus the fine approach of the upper sample is controlled via the applied current to the coil, which in turn is provided by a remote-controlled power supply. The conversion factor for the current set-up is $1.926 \cdot 10^{-2}$ N/A. Due to the current limitation of the magnetic coil this results in a maximum force of 50 mN. For our measurements it is of critical importance that the samples do not perform a rolling motion on each other. Thus the set-up is such that the force is generated at the flexible end of the cantilever, the spring leaf bends and the surfaces are brought into contact by increasing the external force. Once the surfaces are in contact, the spring leaf no longer deforms and an increasing external force results directly in an increasing pressure within the contact area.
In SFA1 the light is fed through thin glass windows in the top and the bottom wall of the cell. Two additional windows in the side walls allow the samples to be viewed thus simplifying the alignment and the injection of the liquid. The liquid is injected with a thin needle and a syringe through a rubber septum in the side wall. To ensure controlled condi-

tions a temperature sensor is installed close to the position of the lower sample inside the centre plate. The electrical connection is via a plug in the top wall. Additionally, two valves in the side wall allow the cell to be flushed with dry nitrogen. During the experiments with octamethylcyclotetrasiloxane (OMCTS), a small container with P_2O_5 acting as drying agent is placed in the SFA chamber.
SFA2 was designed for experiments investigating the in-plane structure of the molecularly thin lubricant layers. This can be achieved with x-ray scattering experiments. With a thickness in the range of a few nanometers the scattering signal of the liquid films is quite small. Therefore it is necessary to optimise the signal to noise ratio. For this purpose the whole set-up was placed in a vacuum pot. For the investigation of the liquid films it is not possible to evacuate the chamber volume, as this would result in the evaporation of the liquid and thus the chamber volume for SFA2 was designed as small as possible. Figure 3.7 shows the design of SFA2. The upper sample in cell SFA2 is rigidly mounted to the top plate, and the bottom surface is mounted onto a piezo-tube. The piezo has a four segment electrode on the outside and thus can be used for both fine approach and applying shear forces (by bending the piezo). The piezo is computer controlled via a DAAD-board in combination with a high voltage amplifier with five independent channels (ElbaTech). It can be displaced ± 8 μm in the horizontal and ± 1.5 μm in the vertical direction and is mounted on a rotation stage which allows the alignment of the lower surface with respect to the upper sample within a range of $\pm 5^\circ$. The wall of the sample chamber is a ring made of teflon. The gap between the ring and the top of the piezo-tube is sealed with a flexible rubber membrane. The top plate is pressed against three micrometer screws with springs. The fine screws allow alignment and coarse approach of the surfaces. One of the micrometer screws is motorised with a pico-motor and can be controlled

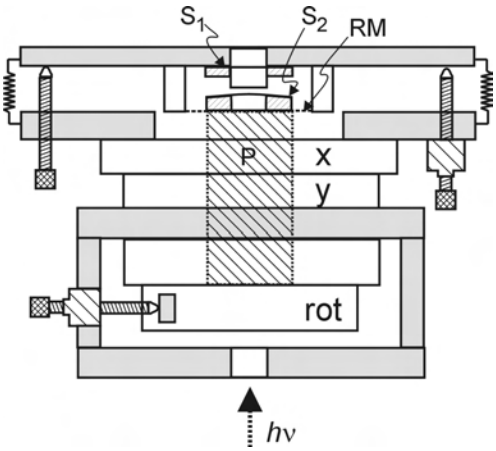

Figure 3.7: Schematic sketch of SFA2 (S_1, S_2: upper and lower sample, RM: rubber membrane, P: piezo (length: 2.5", ∅: 0.5", Staveley Sensors)).

with the computer. One step of the motor corresponds to an approach of the surfaces by 5 nm. In order to change the area of contact on the surfaces the top-plate, including the sample chamber, is mounted on an x-y-translation stage, which allows for a lateral translation by ±3 mm of the top plate relative to the piezo tube. The temperature can be measured with a Pt100 resistor, which is placed inside the top-plate close to the sample position. To ensure dry conditions within the sample chamber again a container with drying agent P_2O_5 can be inserted.
SFA2 was used for x-ray scattering experiments at the ESRF in Grenoble described in detail in Section 6.1. As already mentioned above, the cell was mounted in a vacuum pot to reduce the air scattering. Thus, the method of temperature control described in Section 3.1.3 is not possible. In order to

allow temperature control two heating resistors are mounted to the top plate. This allows at least a change and stabilisation to temperatures higher than the environmental temperature. The heat resistors are connected to a computer controlled power supply and the temperature is controlled in combination with the Pt100 resistor via a purpose-written LabView® program with an integrated PID-control loop.
Two different types of sample supports were used for the experiments in this thesis. One type of sample support involves gluing the samples onto cylindrical lenses made of quartz glass with a radius of curvature of $R_{lenses} = 2$ cm. The lenses are clamped into supports made of stainless steel, whilst the support for the upper sample has permanent magnets. The advantage of the cylindrical lenses is the relatively easy cleaning procedure and sample mounting. An alternative way to assemble the samples was also used and is as follows. Instead of the cylindrical lenses, conventional microscope cover slides with a thickness of approximately 80 μm can be used, which are clamped on stainless steel sample holders. These sample holders can be easily and affordably manufactured with different radii of curvature. For the set-up described here sample holders with radii of curvature of $R_1 = 5$ cm and $R_2 = 7$ cm were made. Here again, the support for the upper sample is equipped with magnets. As well as being affordable to produce, these sample holders offer further advantages in the preparation procedure. The origin of these advantages lies in the flat geometry that is obtainable when the mica surfaces are glued onto the thin glass sheets. This flat geometry makes it possible for the surfaces to be chemically patterned, i.e. with micro-contact printing and also means that the samples are amenable to further characterisation techniques, for e.g. with AFM. Furthermore the thin glass sheets can be used for x-ray scattering experiments, which will be explained below.

3.1.3. Temperature control

For experiments requiring controlled temperatures it is possible to mount the cell inside a thermally insulated box. This box is made of 10 mm thick PVC plates. The inside of the walls are covered with 15 mm thick plates of Styrofoam. Fast temperature changes are possible owing to the small volume of the box ($0.2 \times 0.3 \times 0.2$ m^3). The front wall of the box is equipped with an entrance window for the monochromatic light. The microscope objective penetrates into the box through a hole in the top wall. The gap between the objective and the PVC plate is sealed with a rubber membrane. Inside the box a liquid-air heat exchanger with a low noise fan is mounted. The temperature and flow of the liquid, a mixture of monoethylene glycol and water, is controlled via an external computer operated thermostat. The temperature in the reservoir of the thermostat with this liquid mixture can be adjusted within the range of -30...90°C. The thermostat has an internal proportional-integral temperature controller. It can be controlled either by the reservoir temperature or by an external temperature measured with a Pt100 resistor, as mounted in both SFA cells. A stable temperature, with fluctuations of less than 10 mK, can be obtained for hours at a time. The thermal response time differs significantly in the two SFA cells. SFA1 consists of thick steel walls, which results in a large heat capacity. Furthermore, the thermal contact to the centre plate, where the Pt100 resistor is mounted, is only by air and the points where the plate is in contact with the micrometer screws and the springs. Thus the thermal response time is very long and a change of temperature by 1°C requires 2 to 3 hours for equilibration. In comparison, SFA2 with a much smaller sample volume, is stabilised within approximately 20 minutes for a temperature step of 1°C, if the feedback is set to the sample temperature.

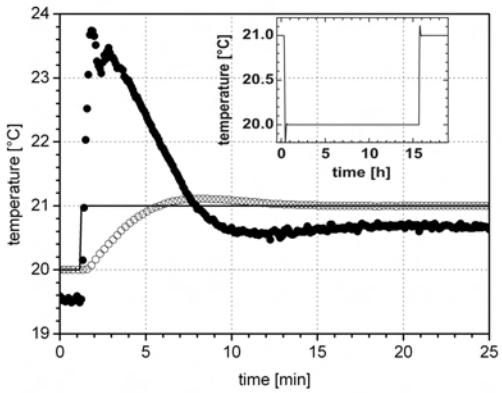

Figure 3.8: Thermal response of SFA2 to a temperature change of 1°C. (closed circles: temperature of thermostat reservoir; open circles: temperature close to sample position; line: setpoint). Inset: Long-time temperature stability of SFA2 measured at sample position.

3.2. Experimental procedures

3.2.1. Sample preparation

To study the behaviour of thin liquid films in confined geometries in the nanometer range, atomically smooth surfaces are required. The contact area in SFA experiments has a diameter of up to 100 μm. Thus for reliable experiments it is necessary to prepare samples with an atomically smooth surface over rather vast distances (≈ 1 cm^2). The only material that provides such high surface quality is mica. Mica is a generic term for a wide range of hydrous aluminum silicate minerals

characterised by a sheet like structure. Depending on its composition it possesses, to varying degrees, the ability to be split into thin sheets. Mica forms flat quasi-hexagonal crystals and the cleavage is parallel to the basal plane. Depending on the chemical composition mica can be classified into a wide range of different types. The only natural micas of commercial importance are phlogopite and muscovite [64]. The substrates used for the work presented in this dissertation were obtained from muscovite mica ($K_2Al_4(AL_2Si_6O_{20})(OH)_4$) exclusively. The basic building unit is a sheet in which each tetrahedrally coordinated cation shares three of its coordinating oxygens with adjacent tetrahedrally coordinated cations. The struc-

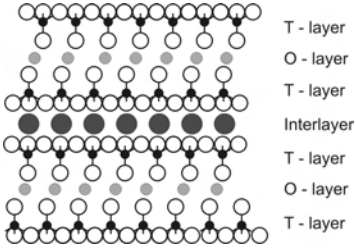

Figure 3.9: Diagram to illustrate the layer structure of mica. The illustration shows a view perpendicular to the plane in which the tetrahedral sheets lie in the mica structure (the (001)-plane).

ture of mica is built of these tetrahedral layers (T-layers), which are stacked with the non-bridging oxygens of one layer pointed towards the non-bridging oxygens of the next layer (see Figure 3.9). Between these two T-layers the non-bridging oxygen atoms form a layer of 6-fold octahedrally coordinated sites (O-layer) and thus these three layers form a T-O-T-layer package [65]. Adjacent T-O-T-layers are stacked with their non-bridging oxygens facing towards each other. Since the

non-bridging oxygens are all bound to two tetrahedrally coordinated cations, they are essentially satisfied when it comes to bonding and contribute little electron density for bonding cations, that lie between two adjacent T-O-T-layer packages. These cations are called interlayer cations and are in large (12-fold) sites with very weak bonds to the adjacent T-layers. These weak bonds to the interlayer cations are the reason for the very good cleavage of mica on their (001)-planes. In the case of di-octahedral muscovite, where only two of the three octahedral sites are occupied, the interlayer consists of potassium cations.
Mica is a birefringent material. The (001) cleavage plane contains the β and γ axes as shown in Figure 3.10 However,

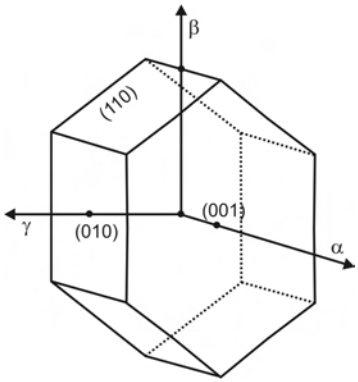

Figure 3.10: Crystallographic axes of mica. The refractive indices along the axes are $n_\alpha = 1.552$, $n_\beta = 1.582$ and $n_\gamma = 1.587$, respectively. [66]

mica is a natural material and the refractive indices can be found in a range of $n_\alpha = 1.552 \ldots 1.570$, $n_\beta = 1.582 \ldots 1.670$ and $n_\gamma = 1.587 \ldots 1.611$ [64]. The dispersion can be taken into account by the parameter b, that one obtains for the

wavelength dependent refractive index [67]:

$$n(\lambda) = n + \frac{b}{\lambda^2}, \tag{3.24}$$

The parameter can adopt values between $b = (4.76 \ldots 5.89) \cdot 10^{-3}$, where λ is expressed in micrometres in Equation 3.24. The usual mica cleaving procedure consists of several successive cleaving steps (see Figure 3.11) and is performed in a laminar flow box to minimise contamination. A large ($\approx 10 \times 10$ cm^2) and thick sheet of as-received mica is cleaved until a sheet, several square centimeters in area and of the order of a few microns thick, is obtained. Using a thin and sharp pin, the mica sheet is initially cleaved along its edge and then is subsequently cleaved carefully by hand. Immediately after cleaving the mica down to a thickness of roughly 10 μm the thin mica sheet is cut into pieces of (1×2 cm^2) with a glowing wire [68–70]. The custom-built cutting set-up used in our experiments consisted of a thin (0.1 mm in diameter) Pt/Ir-wire (80%/20%) attached to an x-y-translation stage. To cut the mica a current is applied until the wire glows bright red. For storage and for the following preparation steps the mica substrates, obtained by the process described above, are placed on a freshly cleaved thick mica sheet, the so-called backing sheet. The backing sheets with the adhered mica substrates are then placed in to a vacuum chamber, where thin silver mirrors are deposited by thermal evaporation. After the silver deposition the substrates are removed carefully with tweezers from the backing sheet in a laminar flow box and are immediately glued with a thermosetting epoxy glue, silver side down, onto a sample holder. In order to do this the sample support is placed on a heating plate and heated to approximately 80°C. A sheet of freshly prepared mica is cut in the middle with a sharp scalpel so that two mica pieces of approximately the same size are obtained. These two pieces are therefore of the same thickness and possess the same orientation of the mica lattice. This must be

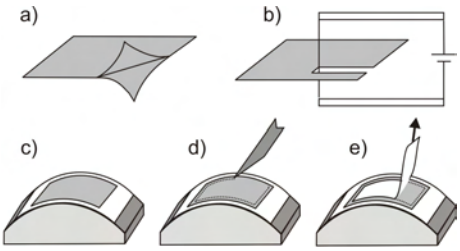

Figure 3.11: Mica preparation method: a) A large piece of mica is cleaved down to a thickness of several μm using a sharp needle. b) The thin mica is cut into small pieces of $\approx (1 \times 2)$ cm^2 with a glowing Pt/Ir-wire. c) The mica pieces are glued with a thermosetting epoxy-glue onto the sample support. d) For the recleaving process the mica samples are cut carefully with a scalpel at their edges. e) Using adhesive tape a few layers of mica are cleaved from the sample.

taken into account when orienting the substrates onto the support. Using the optical birefringence of mica the lattice orientation can easily be confirmed.
The preparation procedure described up to this point was the standard method for most experiments over the last few decades [4, 8, 11, 12, 14]. Recently it was found that the prepared mica surfaces, which are supposed to be clean, are in fact contaminated by small particles [69]. These nanoparticles are typically 20-25 nm in diameter and 2-3 nm high and arise from the cutting process with the glowing platinum wire. Atomic force microscopy images have been taken from the prepared mica samples and indeed the results showed that the surfaces were not atomically smooth, but instead were covered with small particles (see Figure 3.12). The degree of coverage depends on the thickness of the mica sheet cut with the platinum wire. Obviously, on a nanometer scale, these

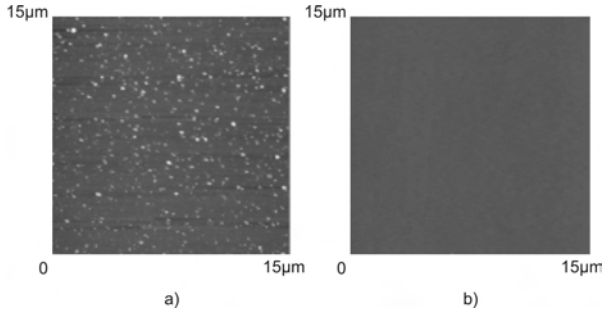

Figure 3.12: AFM images taken from the prepared mica samples. In a) the surface was prepared using the standard procedure. Here, clearly the nanoparticles due to the hot wire cutting can be seen. The particles have a height of a few nanometers and a diameter of a few tens of nanometers. b) After performing the re-cleaving step, the surface is free of these nanoparticles.

nanoparticles influence the behaviour of the adjacent liquid dramatically. SFA measurements performed with these surfaces may lead to erroneous interpretations.
In the past, different methods to prevent this surface contamination were presented [68, 71, 72]. To obtain contamination free samples for our experiments, a procedure based on the method first presented by P. Frantz and M. Salmeron [68] was used. The original motivation for their novel preparation method was based on eliminating organic layers on the mica surface. Even mica surfaces that have been carefully prepared in a laminar flow box will have contamination due to adsorption of carbon compounds originating from the ambient air. In order to eliminate this contamination, they developed a tape-cleaving technique. For that relatively thick mica samples (between 4 and 8 μm) were prepared with the standard procedure. After evaporating the Ag mirror they were glued on silica lenses and a piece of adhesive tape was

applied to the mica surface. Immediately before the experiment the mica samples were recleaved by peeling off the tape. A slightly modified version of this technique has been further developed by us and is described in following paragraph (see also Figure 3.11 d)-e)).
After gluing the mica pieces to the support, the substrates are cut with a scalpel very carefully along their edges. Immediately prior to the experiment, a piece of adhesive tape is used to re-cleave the mica carefully. These steps can be repeated a few times and guarantee a freshly cleaved mica substrate. The surfaces obtained with this procedure are free of any contamination due to the preceding preparation steps. In particular, the surfaces are free of nanoparticles (see Figure 3.12b)). Furthermore absorbed organic molecules from the ambient atmosphere are removed with this re-cleaving step. Mica sheets with a thickness of only a few micrometers are very difficult to handle. These very thin mica foils flutter in the air-flow of the laminar flow chamber and often fold up. Furthermore it is difficult to take the mica samples from the backing sheet after the silver deposition, without disrupting them. Also, if the epoxy glue layer is not thin enough the very thin mica sheets have a tendency to wrinkle uncontrollable and thus make it difficult to obtain a smooth surface topography. All these problems can be avoided with the re-cleaving technique. Here, the mica samples can be prepared with a thickness between $10 \ldots 20$ μm. This allows for much easier handling and also means that the surface topography is well defined. Once a thick layer of glue is molten on the support, the mica sheet spreads the glue effectively underneath it to adopt a curvature identically to the support. To obtain a good optical resolution, the combined thickness of both mica samples should be in the range of $d_{Mica,total} \approx 1 \ldots 6$ μm. Different thicknesses of the substrates can be obtained by several successive re-cleaving steps.
The only disadvantage compared to the conventional tech-

nique is the loss of the symmetry of the system. In experiments without the re-cleaving procedure the upper and the lower sample are of the same thickness and the system is symmetric. In the re-cleaved system this symmetry is lost. For a measurement of the absolute change in distance of separation between the surfaces it is therefore necessary to determine the asymmetry A between both samples. A definition of this asymmetry A and its influence on the measurements will be given in section 4.1.1.

3.2.2. OMCTS

The experiments in this dissertation were all performed with octamethylcyclotetrasiloxane (OMCTS) with the chemical structure formula $(SiO)_4(CH_3)_8$. OMCTS has already been

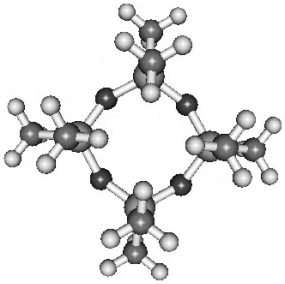

Figure 3.13: OMCTS molecule

used in earlier investigations by others [5, 11, 12, 14, 15, 73] and is thus well established as a model liquid for SFA experiments. This non-polar silicone oil has reasonably rigid, quasi-spherical molecules as shown in Figure 3.13. More pre-

cisely, the molecule is an oblate spheroid of major diameter of 1.0-1.1 nm and minor diameter of 0.7-0.8 nm, respectively [8]. OMCTS is inert and has a low dipole moment of $\mu = 0.42$ D [5] and with a melting point of $T_{mp} = 17.5°C$ is liquid at room temperature. The dielectric constant is $\epsilon = 2.3$ and the refractive index is $n = 1.3968$. A summary of the properties of OMCTS is shown in Table 3.1. In contrast to experiments

Table 3.1: Properties of Octamethylcyclotetrasiloxane (OMCTS)

Molecular formula	$(SiO)_4(CH_3)_8$
Molecular weight	296.62
density ρ	0.956 g/cm^3
melting point	17-19°C
boiling point	175-176°C
vapor pressure (20°C)	0.93 mbar
water solubility	56 ppb
surface tension σ	18.796 mN/m
dipole moment μ	0.42 D
dielectric constant ϵ (20°C)	2.318
refractive index n (20°C)	1.3968
bulk viscosity η (25°C)	2.2×10^{-3} Pas

performed by other groups the liquid was not distilled for our investigations. OMCTS was used as received with a degree of purity of $\geq$99%. The impurity level, in particular of non-cyclic molecules was below the detection level of NMR-spectroscopy [1]. The effect of water concentration in OMCTS plays an important role for the observation of the molecular layering transitions. H.K. Christenson *et al.* performed

[1] The NMR measurements were performed by the group of Prof. Dr. K. Landfester, Department of Organic Chemistry III, University of Ulm

measurements of the solvation force between mica surfaces in a SFA across a thin film of OMCTS with different concentrations of water [5, 49]. The thermodynamically significant quantity for the water concentration is the activity a_w. The water activity a_w is proportional to the mole fraction and is equal to one for a saturated solution. For increasing water activity they observed a decrease of the amplitude of the oscillating solvation force. Furthermore, some of the inner oscillations were found to be inaccessible for the measurements and the adhesion at the contact area of the mica surfaces increased dramatically with increasing a_w. It is known that in binary mixtures of OMCTS with smaller molecules the range and the amplitude of the oscillating force profile are reduced. For instance, this is the case for a mixture of OMCTS and cyclohexane [33] and can be understood in terms of simple packing of the molecules. But in the case of water and OMCTS it is different. The observations can be described with two separate effects. A higher water concentration in the OMCTS results in an increased excess of water at the surface. Due to the polar character of mica and water, water exhibits a greater affinity to mica than OMCTS (which has a small but nonzero contact angle on mica [49]). Thus, discrete water molecules adsorb on the surface, which may lead to a kind of surface roughness effect. This disrupts the molecular ordering of the OMCTS molecules due to the confining mica surfaces [49]. As a consequence, the long range forces smear out with increasing surface separation. The second effect is a phase separation or spontaneous condensation of water at large surface separations. This leads to sudden jumps of the surfaces into contact from a separation equivalent to three molecular layers and to a very large contact adhesion.
Here, we are interested in the observation of the collapse dynamics of liquid layers depending on the number n of confined molecular layers, especially for $n = 5 \ldots 1$. Measurements of the water content of the received OMCTS using Fischer titra-

tion yielded 63 ppm water. Because of the significant effect of water described above, the OMCTS was stored for 2 to 3 days over a 4 Å molecular sieve to extract the residual water. After this treatment a water content of only 3 ppm was measured. The experiments were then performed with a container of phosphorous pentoxide inside the SFA-chamber to assure water activity of $a_w = 0$.

3.2.3. The experiment

After installing the samples into the SFA-cell the cell itself is flushed with dry nitrogen to obtain controlled environmental conditions. The dry atmosphere is also necessary to make sure that the samples are not disrupted as a result of the very strong adhesion that occurs in the presence of adsorbed water from humid air. Then the mica surfaces are brought into contact and the transmission through the system is recorded depending on the wavelength. To determine the thickness of the samples at least two transmission peaks have to be recorded. Due to the sensitivity of the CCD-camera, these transmission spectra can be taken in the range between 400 and 600 nm. From the position of these peaks the thickness is calculated using the FSC technique, described in Section 3.2.4.
In the beginning of an experimental run, two-dimensional transmission images were acquired for a range of wavelengths and saved to disk, that one obtains a three dimensional set of data (with the x- and y-axis of the transmission images and the wavelength λ as coordinates). Figure 3.14 shows a typical transmission image of two mica surfaces in contact, which is in principal a cut through the 3d set of data at a certain λ_0. In this image, the wavelength was adjusted to the wing of a transmission peak of the contact area. In the centre of this image, the roughly circular area of contact can

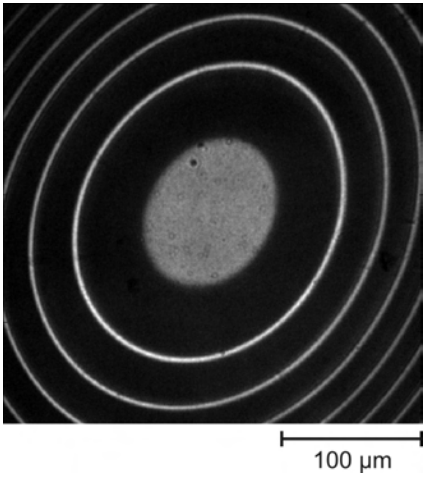

Figure 3.14: A typical transmission image of two mica samples in contact. The wavelength is adjusted to the wing of a transmission peak of the system. The wavelength distribution due to the adjusted slit width at the exit of the monochromator is $\Delta\lambda = \pm 2$ nm around λ_0. Due to an elastic deformation the samples are flattened in the contact region. The homogeneous gray level of the contact area reflects the uniform thickness between the silver mirrors. Outside the contact area Newton fringes can be seen. The lateral separation between the fringes is determined by $\frac{\lambda}{2} = n\Delta d$.

be seen. Here, the distance between the outer silver mirrors is uniform due to an elastic flattening of the substrates. This uniformity is represented in the image by a homogenous gray level. Around the contact area Newton fringes are observed. The distance between two adjacent fringes is equivalent to a change in gap distance of half the wavelength times the refractive index, $\lambda/2 = n\Delta d$. Due to the crossed cylinder configuration of the samples, which is equivalent to a sphere on a flat surface, the lateral separation between adjacent New-

ton fringes becomes smaller for increasing distances from the contact area. In order to extract thickness information, the

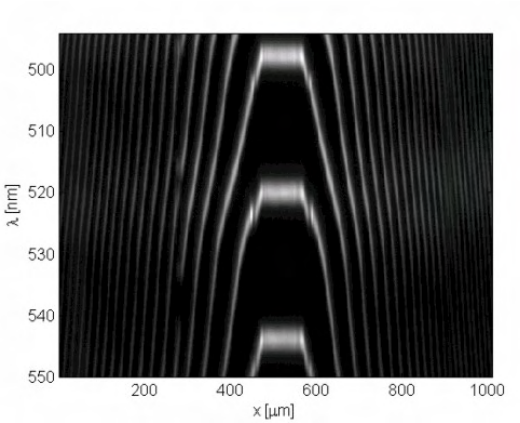

Figure 3.15: Cross section through the 3d dataset at a certain x-coordinate in the contact area. This representation is similar to conventional FECO data. The straight segment represents the contact area. The break in the fringes on both sides of the contact area is due to a capillary liquid neck. The shape of the fringes provides information about the monochromatic order.

intensity of the transmitted light inside the contact area is plotted against the wavelength λ. The intensity is usually averaged laterally over an area of approximately $(5 \times 5)\ \mu\mathrm{m}^2$ in order to reduce noise. The result is a transmission spectrum of the contact area, where the thickness can now be calculated from the peak positions.
In order to save time and disk space, the transmission spectrum can be recorded in a different way. Instead of recording complete transmission images, the intensity averaged over 5 horizontal lines is recorded depending on the wavelength. This results in a $(m \times n)$-matrix, where n is the number

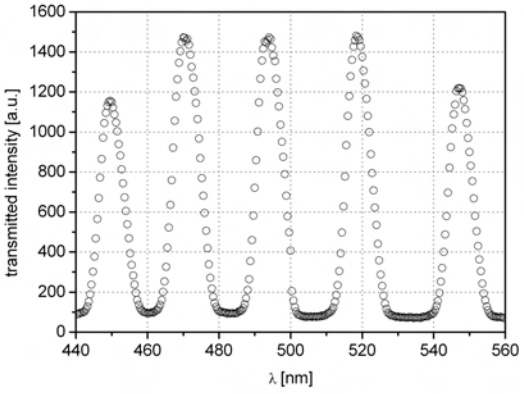

Figure 3.16: Cross section through the 3d dataset through a certain x-y-area in the contact area. The intensity in the area is averaged and then plotted versus the wavelength. From these plots it is possible to determine the thickness of the system (see Section 3.2.4).

of horizontal pixels and m is the number of measurements at different wavelengths. The matrix can be displayed as a 2-dimensional image, in which the x-axis represents the lateral position in the transmission image and the y-axis is the wavelength λ. This kind of plot is identical to the FECO-technique and is shown in Figure 3.15.
In the plot shown in Figure 3.15 one can see the following. The straight segment at a lateral position between 500 and 600 μm represents the contact area. The break in the fringes close to the contact area is due to a liquid neck formed by capillary condensation of OMCTS. The order of the fringes can be seen by the shape of the intensity [74]. In the present two-dimensional representation the upper fringe at $\lambda \approx 497$

nm is of odd order, and the next fringe at $\lambda \approx 520$ nm is of even order. To obtain a wavelength spectrum to determine the thickness of the system, vertical cross-sections can be extracted from these two-dimensional representations of the spectral data versus one spatial coordinate (see Figure 3.16).

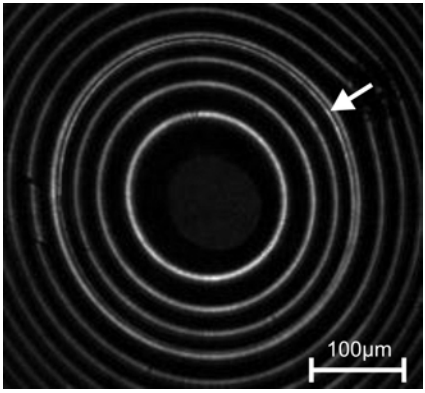

Figure 3.17: Formation of OMCTS neck due to capillary condensation. The image was taken approximately 8 minutes after injecting the liquid (T=23°C). The additional fringe (indicated by the arrow) refers to the edge of the liquid neck.

After the acquisition of the reference spectra of the samples in dry contact, the liquid is injected into the SFA-cell with a syringe. OMCTS is injected not directly onto the mica surfaces, but instead onto the centre plate of the SFA close to the sample position. The advantage of this method is that no mica particles (possibly created during the re-cleaving process) are able to flow over the surfaces. Instead, the liquid is transported to the sample surface via the vapour phase. During and after the injection process, the surfaces must remain in contact. Then, due to capillary condensation,

the OMCTS condenses in the pore generated at the edge of the contact area. This results in the formation of a liquid neck around the contact area within the first few minutes after the injection. The growth rate of the liquid neck depends on the vapour pressure of the liquid used. Figure 3.17 shows an image taken after the injection of OMCTS into the SFA-cell. The temperature in this experiment was adjusted to $T_{SFA} = 23°C$. The wavelength of the incident monochromatic light was adjusted in order to visualise the liquid neck. After approximately one hour the diameter of the liquid neck is about 0.5 mm at room temperature. At this stage, the surfaces are separated using the magnetic force generated by the coil on top of the cell and brought again together at a separation of a few microns. The system is then stabilised for a few minutes at this separation.

3.2.4. Data analysis

The total thickness of the mica samples and subsequently the thickness of the confined liquid films is calculated from the recorded transmission spectra. In order to do this the so-called Fast Spectral Correlation (FSC) method, originally developed by Heuberger *et al.* [75], is used. A short description of this numerical tool (based on [75, 76]) which allows the quick and precise analysis of the measured spectra will be given in the following.
The aim of this method is to determine the thickness of the system by fitting the transmission spectrum. It would require a large computational expense to perform a fitting routine to the complete experimental transmission spectrum. The FSC method reduces this expense enormously. Here, only the wavelengths of the transmission peaks are used for the fitting routine. The fitting parameter in our case is, for example, the total thickness of the mica samples $d_{mica,tot}$ in dry con-

tact. The correlation is maximised by finding an appropriate value for $d_{mica,tot}$. For this purpose the wavelengths of the peaks in the measured transmission spectrum are extracted. The peak detection is performed with an algorithm written in MatLab. Setting a certain intensity threshold value results in a number of pixel arrays with intensity values above the threshold. Each array corresponds to one transmission peak. The maximum value of the peaks are found by a polynomial fit of 5th order to every single array. The result of the peak detection algorithm is a vector $\vec{\Lambda}$ containing the wavelengths of the transmission maxima:

$$\vec{\Lambda} = \begin{pmatrix} \lambda_1 \\ \lambda_2 \\ \vdots \\ \lambda_N \end{pmatrix} \tag{3.25}$$

For the thickness determination using FSC the transmission $T(\lambda_i, d)$ is calculated only at the wavelengths given with $\vec{\Lambda}$ with d being the parameter. For every thickness value the value for the FSC function T_{FSC} is calculated as the sum of the calculated transmission at the wavelengths λ_i for the thickness d:

$$T_{\mathrm{FSC}}(\vec{\Lambda}, d) = \sum_{i=1}^{N} T(\lambda_i, d) \tag{3.26}$$

If the corresponding refractive index n of the medium is known, the FSC function T_{FSC} is the fitting argument for the determination of the thickness d. Figure 3.18(a) displays the plot of T_{FSC} against d for a calculated transmission spectrum with the transmission peaks at λ_i (see Figure 3.18(b)). The sharp peak represents the thickness, where the correlation is maximised.
FSC can also be applied for the simultaneous determination of two parameters, e.g. within the scope of this thesis the asymmetry A of the mica substrates (see Section 4.1.1) and

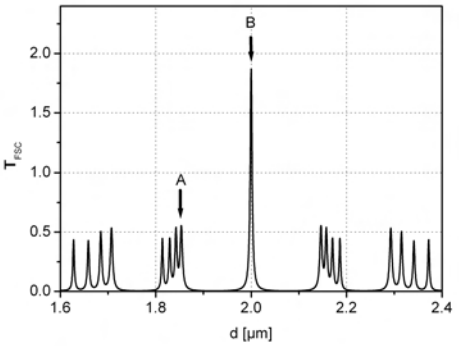

(a)

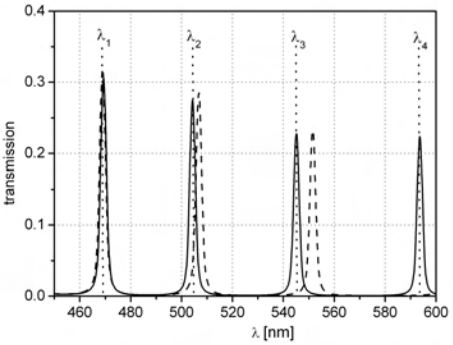

(b)

Figure 3.18: Principle of the FSC method. Using the matrix method the transmission is calculated for the parameter d at the peak positions λ_i extracted from an experiment. The value of T_{FSC} is the sum of the transmission calculated at λ_i, where i numerates the number of transmission peaks. A maximum correlation is obtained for the thickness denoted with B in (a). The corresponding transmission spectrum is represented with a solid line. The dashed line shows the spectrum calculated for the value at position A.

the thickness of the liquid film. For this it is necessary to know the total thickness of the substrates in dry contact and the refractive index of the liquid. The result of the FSC in this case is a two-dimensional plot as is shown in Figure 3.19.

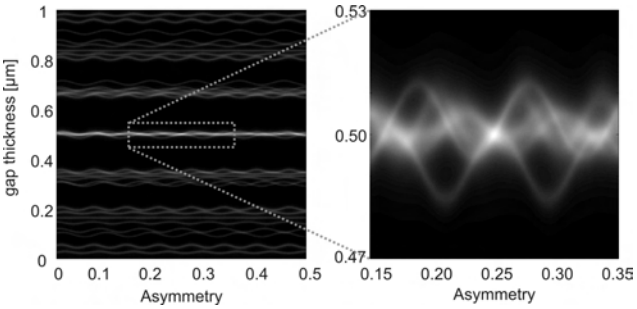

Figure 3.19: Two dimensional representation of the FSC function for the evaluation of gap layer thickness and substrate asymmetry. The peak positions are extracted from a calculated transmission spectrum ($d_{mica,tot} = 2$ μm, $A = 0.25$, $d_{Gap} = 500$ nm, $n_{Gap} = 1.396$).

4. Optical sample characterisation

At the beginning of each experiment the samples must first be characterised. In particular, the total thickness of the upper and lower mica sheet has to be determined, when they are in contact. The asymmetry A of the upper and lower sample is an important parameter for the determination of the thickness of the confined liquid films. The procedure for analysing the asymmetry of the mica samples and thickness of both samples and liquid film, will be described in Section 4.1.1.
Importantly, in this chapter, the results of the measurements with the two-dimensional imaging SFA will now be presented. First, the properties of the mica samples investigated from a transmission spectrum in dry contact will be discussed. With these results, the thickness of media confined between the mica sheets and, in particular, the thickness of thin liquid films can be determined. The film thickness for different numbers of molecular layers can be measured via the FSC method (a technique described in detail in Section 3.2.4) or the change in thickness for one expulsion process can be obtained from the change of intensity of the transmitted light through the area of contact.

4.1. Mica substrates

Independent of the method of data acquisition, either with full image acquisition or with the FECO-like technique, the final set of data required for the determination of the thickness of the system is a wavelength spectrum, as shown with open circles in Figure 4.1.

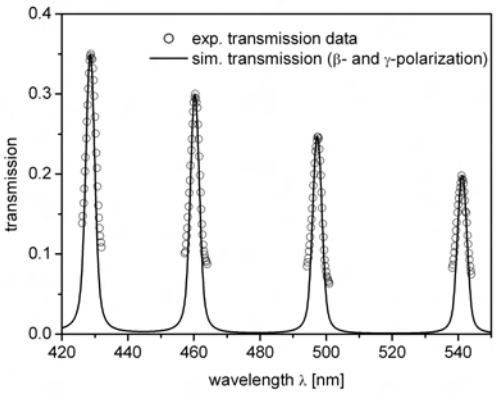

Figure 4.1: Experimental transmission spectrum (open circles). The solid line represents the calculated transmission spectrum including $\beta-$ and $\gamma-$polarisation for the total mica thickness of $d_{Mica,tot} = 1.8159$ μm.

From the wavelength of the transmission peaks the thickness of the substrates in dry contact is then calculated using the FSC technique, as described in section 3.2.4. Figure 4.2 shows the resulting plot of the FSC analysis. The value of $d_{Mica,total}$ =1.8159 μm for the thickness at the position of the peak represents the mica thickness with the best correlation between the experimental data and the calculated transmis-

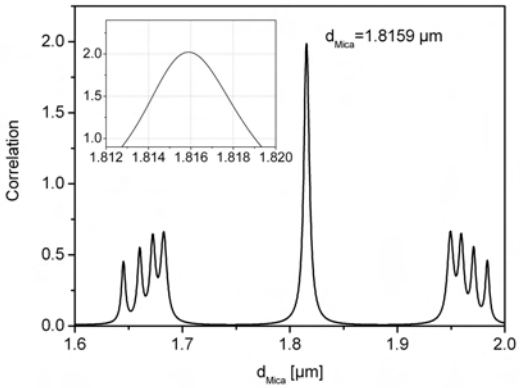

Figure 4.2: The result of FSC analysis for the transmission peaks of Figure 4.1. ($\lambda_1 = 428.85$ nm, $\lambda_2 = 460.43$ nm, $\lambda_3 = 497.46$ nm, $\lambda_4 = 541.12$ nm; silver mirror $d_{Ag} = 45.1$ nm).

sion spectrum. In the next step, the transmission spectrum for the system is calculated with this value for the total mica thickness and compared with the experimental data. The absolute positions of the peaks are already in good agreement when only one refractive index is included for the calculation. The deviation between the experimental and the calculated peaks is typically less than 1 Å. The result is a thickness resolution for the current system on the order of 0.2 nm. Although the wavelength distribution of $\Delta\lambda = \pm 2$ nm due to the adjusted slit width on the monochromator is included in the calculation, there is still a discrepancy in the width of the experimental and the simulated transmission peaks. The reason for this deviation can be explained by the birefringence of the mica. The illumination for this experiment was performed with non-polarised light. Therefore it has to

be taken into account that both refractive indices n_β and n_γ [77, 78] of the mica contribute equally to the transmission. The birefringence results in a peak separation for the β- and the γ-polarisation of the incident light. Figure 4.3

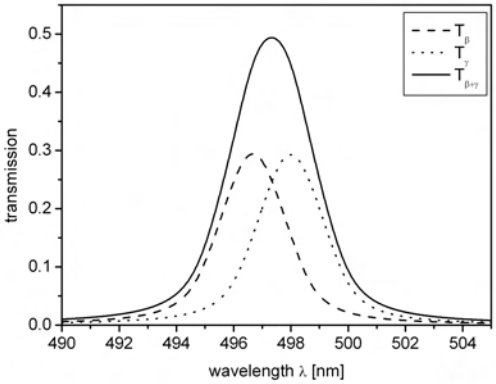

Figure 4.3: Simulated transmission for β- and γ-polarisation ($n_\beta = 1.5794 + 4.76 \cdot 10^{-3}\ 1/\lambda^2$ and $n_\beta = 1.5838 + 4.76 \cdot 10^{-3}\ 1/\lambda^2$). Using unpolarised light yields the sum of both and thus to a broader peak than expected from the wavelength distribution from the monochromator. The separation between the β- and the γ-peak is 1.3 nm

displays the separately calculated transmission for both polarisations. The separation $\Delta\lambda_{\beta\gamma} = \lambda_\beta - \lambda_\gamma$ between the β- and the γ-peak depends on the birefringence $\Delta n = n_\beta - n_\gamma$ of the mica and the wavelength and can be obtained from

$$\Delta\lambda = \frac{\Delta n}{n_\gamma}\lambda_\gamma, \tag{4.1}$$

whereas λ_γ depends on the thickness of the mica. Calculating the sum of both peaks is equivalent to the case of a measure-

ment with unpolarized light (solid line). The width of the resulting peak is obviously larger than the width of a peak calculated with just one refractive index and the wavelength distribution $\Delta\lambda$. A comparison of the calculated transmission (including the birefringence of the mica) with the experimental data is shown as a solid line in Figure 4.1. Now, the peak position and the width of the transmission peaks are in very good agreement. Concerning the measured absolute transmitted intensity (i.e. the peak height) deviations from the calculation with the matrix method were found. These deviations are probably related to the dispersion function of the Ag mirrors. The dispersion function was taken for evaporated films from the literature [63] but we did not measure it in separate experiments. However, it was checked that these deviations can be neglected for the determination of the mica and liquid film thickness. To obtain a better comparison between the experimental and calculated data the intensity of each experimentally measured peak in Figure 4.1 was normalised independently to the height of the corresponding calculated peak.

4.1.1. Substrate asymmetry

Due to the tape re-cleaving procedure used to obtain particle-free mica surfaces, the thickness of the upper and lower sample are different. For an accurate determination of the thickness of a thin liquid between the mica sheets this asymmetry is of crucial importance. Two independent methods were used to determine the asymmetry A, which is given by Equation 4.2. Here, d_1 and d_2 denote the thickness of the upper and lower mica sheets, respectively.

$$A = \frac{d_1}{d_1 + d_2} \tag{4.2}$$

The first method is to extract a wavelength spectrum from a position outside the contact area from the dry λ-scan. Here, the system consists of the mica sheets with different thickness and an air gap in between them. Thus the refractive index of the gap is known and the FSC can be performed with the gap width d_{Gap} and the asymmetry A as parameter. The result can be seen in a two-dimensional image (see Figure 3.19 in Section 3.2.4). The value of correlation is represented by the gray level. This can be performed for a set of different lateral positions.
Another way to measure the asymmetry of the upper and lower sample can be performed after the experiment is finished. After cleaning the surfaces from the liquid used, by rinsing them with ethanol, a further silver mirror is evaporated onto the topsides of both samples such that each sample independently is a Fabry-Perot interferometer. Now, the wavelength spectra can be recorded and analysed for both samples separately.
The quality of the agreement of the both presented methods was not the same through all experiments. The difficulty in the method of coating the samples with a second Ag mirror is to clean the sample surfaces from any contamination to obtain an Ag mirror directly on the mica and not on some contaminating layers. Furthermore the set-up is very sensitive to the optical alignment. Therefore special care has to be taken while demounting the samples for the Ag evaporation. For very thin samples, in particular with a large asymmetry, it was not possible to measure the upper and lower sample separately, because no transmission peak was found within the acquisition range (λ=400...600 nm) of the set-up. Problems with the FSC method may arise from focussing of the video microscope. For the measurements presented in this work, usually both methods were used to obtain qualitatively good information.

4.2. OMCTS film thickness

To determine the thickness of confined liquid OMCTS films, two different measurements are possible with the present set-up. Either the change in transmitted intensity for changing film thickness can be transformed into a thickness profile or the technique of FSC can be used. The following section presents both methods for obtaining numerical data from the experiments. The main difference between both measurements is the acquisition speed of the data and the range of thickness variations that can be recorded. Measuring the changes in intensity allows a high image acquisition but restricts the range of the thickness variations. On the other hand, with the FSC method any change in thickness can be measured, but the FSC is not suitable to measure fast changes in the thickness.

4.2.1. Load ramps - changes in intensity of transmitted light

To record the dynamics of the collapse of the liquid films confined between the mica samples, the wavelength λ_0 of the incident light is adjusted to one of the wings of a transmission peak in the reference spectrum of the system. When the film thickness changes, the wavelength λ_p of the transmission peak shifts. As a consequence, the transmitted intensity at a given fixed wavelength decreases or increases, depending on the relative values of λ_0 and λ_p. This preserves the high resolution concerning the film thickness. Once the wavelength is adjusted to a certain value, load ramps can be applied via the magnetic coil. Figure 4.4 shows snapshots from a video sequence of an experimental run. Here, a continuously increasing load ramp presses the surfaces together. The first obser-

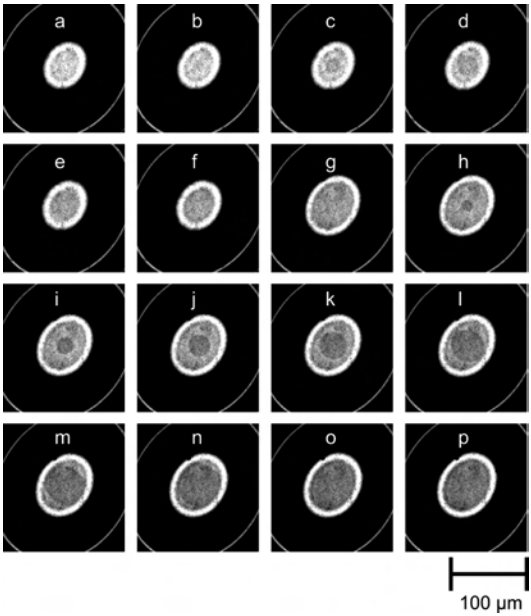

Figure 4.4: A series of snapshots of two subsequent expulsion processes. Darker gray level corresponds to thinner film thickness. The area of contact increases due to an elastic flattening of the substrates. At the edge of the images the next order Newton fringe is visible. Time between images: a-f: $\Delta t = 50$ ms, g-p: $\Delta t = 100$ ms.

vation during this experiment is that the increasing external force results in an elastic flattening of the contact area. The contact area in typical experiments has a diameter of approximately 50 to 100 μm at the highest load of approximately 14 mN. In Figure 4.4c) and h) darker spots appear close to the centre of the contact area. These darker spots subsequently spread over the contact area. In this experiment, the wavelength was adjusted to the right side of a transmission peak in the reference spectrum. As a consequence, a decreasing transmission through the system corresponds to a decreasing film thickness. The reason that the nucleation occurs in or close to the centre can be seen from Equations 2.7 and 2.8. The elastic relaxation energy is proportional to P^2/E. Since the pressure P is at maximum in the centre, the system gains the most energy for a generation of the island with thickness n-1 in the centre of the contact area.
The diagram in Figure 4.5 shows the transmitted intensity averaged over an area of (5×5) μm^2 within the contact area as a function of increasing load with time. For large surface separations in the beginning of the experimental run, the intensity varied continuously. As the surfaces came closer together, a series of discrete steps appeared. As already mentioned the wavelength for this experiment was adjusted to the right wing of a transmission peak of the reference spectrum. Thus, decreasing film thickness results in a decreasing value of transmission, because the transmission spectrum is shifted to smaller wavelengths. Between the intensity steps in Figure 4.5 the transmitted intensity remains more or less at a constant value. This corresponds to a constant film thickness between the steps. From the change in intensity it is now possible to determine the change in thickness between the mica samples. Using the total mica thickness $d_{Mica,total}$, determined from the reference spectrum in dry contact, the transmitted intensity $I_T(\lambda_0)$ as function of the liquid film thickness d_{liquid} can be calculated. To transform the intensity

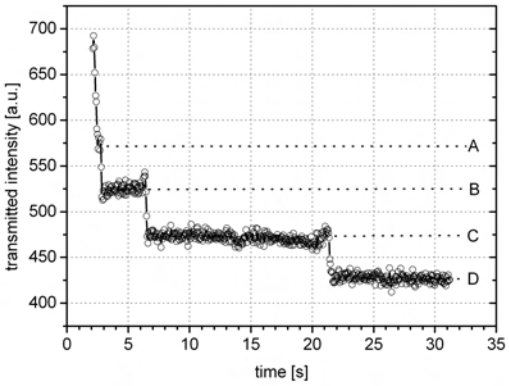

Figure 4.5: Transmitted intensity within the contact area versus time during an applied load ramp. The intensity is averaged over an area of (5×5) μm^2 and the image acquisition rate is 19.2 images per second. The wavelength is adjusted to the right side of a transmission peak ($\lambda_0 = 499.0$ nm). The dotted lines indicate the plateau values.

into thickness information, a constant bulk refractive index for the OMCTS has been assumed. Comparing the results of the calculation with the measured time dependent transmission during a load ramp, we obtain the thickness profile of the OMCTS film in between the mica samples shown in Figure 4.6. In this experimental run discrete changes in the OMCTS film thickness from 3.27 nm $\rightarrow$ 2.57 nm $\rightarrow$ 1.96 nm $\rightarrow$ 1.52 nm have been observed. These values are calculated with a resolution of $\pm$ 0.2 nm. The observed decrease per expulsion process is slightly smaller than has been previously found in similar experiments with the same system [11,12,14,49]. But it should be noted, that in contrast to these experiments, the

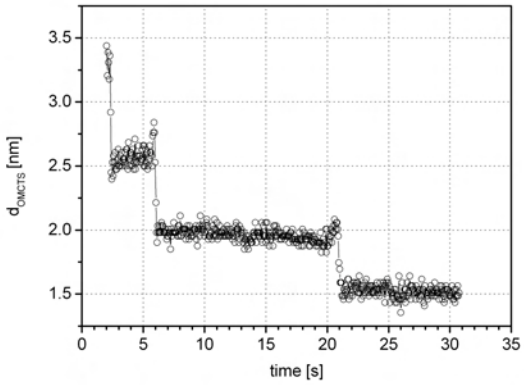

Figure 4.6: Thickness of the OMCTS film versus time. The profile is calculated from the reference spectrum of the sample and the intensity-steps shown in Figure 4.5.

data presented here were measured at a substantially higher pressure (≈ 20 MPa). Furthermore, as already mentioned, a constant refractive index for OMCTS was assumed.

4.2.2. Fast Spectral Correlation on OMCTS

As described above, the FSC technique is a powerful instrument for the data analysis of SFA experiments. During an experiment it is possible to stop the load ramp at various loads corresponding to the plateaus shown in Figure 4.5 and 4.6. The system can be stabilised at a certain number of layers between the mica sheets for several hours. Here, no significant aging effect was observed. Once the system is adjusted to a certain film thickness, transmission spectra in narrow

ranges around the transmission peak can be recorded with high accuracy. Figure 4.7 shows such a measurement for one of the transmission peaks at different film thicknesses. As ex-

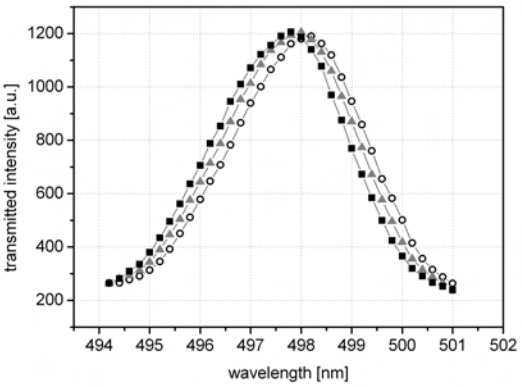

Figure 4.7: Transmission spectrum of a peak at different film thickness. The peaks were recorded at the plateau values in Figure 4.5: Circles: plateau B; Triangles: plateau C; Squares: plateau D

pected, the transmission spectrum is shifted towards smaller wavelengths with decreasing number of liquid layers between the substrates. This again highlights the origin of the steps of transmitted intensity in Figure 4.5. Adjusting the monochromator to a fixed wavelength λ_0, the corresponding intensities to the plateaus B, C and D (in Figure 4.5) can be found. Applying the FSC technique to the obtained transmission peaks results in the values for the OMCTS film listed in Table 4.1. Comparing the results of the FSC with the values obtained from the intensity-profile we find good agreement within the resolution of the system. The value calculated for plateau A from the transmitted intensity was not accessible for the FSC

Table 4.1: Thickness of OMCTS layers obtained from intensity profile and FSC.

Plateau	Intensity-profile	FSC
A	3.27 nm	–
B	2.57 nm	2.63 nm
C	1.96 nm	1.86 nm
D	1.52 nm	1.33 nm

analysis. The reason for this is that it was not possible to stop the load ramp and stabilise the system at this OMCTS thickness. Apart from the fact that the FSC method tends to result in smaller absolute values than the the calculation from the intensity-profile, both measurements yield the same steps in film thickness for the expulsion processes. This confirms the observation, that the change in film thickness for the last recorded transition seems to be significantly smaller than the diameter of the OMCTS molecule. Figure 4.8 compares the data obtained with the FSC method from different experimental runs with different samples. The reduction in film thickness upon expelling on e layer of liquid varies from $(0.58 \ldots 0.86)$ nm. With these measurements of the liquid film thickness it is possible to relate the measured the number of molecular layers confined between the mica surfaces in the two-dimensional imaging SFA. Concerning the measured values from the different measurements one can conclude, that the film thickness can be determined with an accuracy of ± 0.2 nm. The knowledge of the film thickness and thus the number of confined liquid layers is important for the analysis of the dynamics of expulsion processes of single molecular layers that follows in the next chapter.

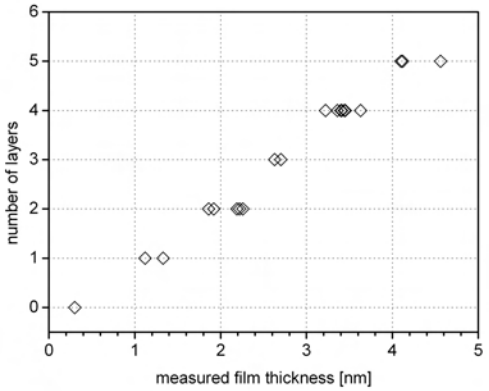

Figure 4.8: Measured film thickness of OMCTS versus the estimated number of confined layers from different experiments.

5. Dynamics of layer expulsion processes

The key advantage of the SFA set-up constructed here is the capability of two-dimensional image acquisition in real-time. As shown in the previous chapter, it then becomes possible to observe the expulsion of single liquid layers out of the contact area. In the work presented in this chapter we observe different drainage scenarios depending on substrate elasticity and applied load ramps. The dynamics of the measured expulsion processes are compared with the simple Persson-Tosatti (PT)-model (described in detail in Section 2.2.3). Furthermore, the effective friction coefficient that is obtained is analysed using an extended hydro-dynamic model.

5.1. Thick substrates

As mentioned above, different scenarios of the expulsion of single liquid layers can be observed using the two-dimensional imaging SFA. The dynamic measurements presented in this section were obtained from experiments with thick mica samples (≥ 1.8 μm) and moderate approach rates.

5.1.1. Dynamics of the boundary line: experiment versus theory

Figure 5.1 shows a series of consecutive images of a video sequence taken from an experimental load ramp of approximately 0.3 mN/s. The total thickness of the mica substrates in this set of measurements was $d_{Mica,total} = (2.3454 \pm 0.0091)$ μm. The wavelength of the incident light was adjusted to the left wing of a transmission peak, i.e. to the short wavelength wing. Thus, increasing intensity corresponds to decreasing film thickness. The layer expulsion shown in Figure 5.1 is the $n = 4 \rightarrow 3$ transition. The first images display the area

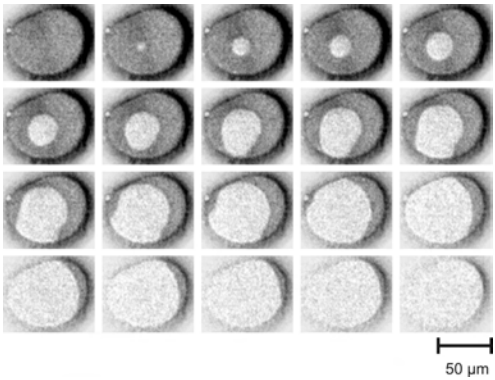

Figure 5.1: Snapshots of the collapsing of layer $n = 4$. Brighter gray level corresponds to decreased film thickness. The dark rim on the right hand side of the images is related to imperfections in background subtraction in conjunction with contrast enhancement. Time between images: Δt =150 ms.

of contact with a metastable liquid film consisting of $n = 4$ layers of OMCTS molecules. The contact area is slightly elliptical because the upper and lower sample are not mounted

in a crossed cylinder geometry at exactly 90°. By the next image, close to the centre of the contact area, a bright spot and thus an island with reduced film thickness n=3 appears. Within the following three seconds this bright area spreads over the whole contact region. Initially the region with $n = 3$ layers of OMCTS is approximately circular. As the boundary line approaches the edge of the contact area, it deforms progressively and adopts a negative curvature at some sections. This double-S-shape can be explained as follows [2,6,18]. As shown in Section 2.2, the growth of the area with reduced number of layers is governed by a potential flow in terms of two-dimensional hydrodynamics. In Figure 5.1 the nucleation does not occur exactly at the centre of the contact area, but slightly off-centred. Therefore the two-dimensional pressure gradient and thus the driving force is larger where the boundary is closer to the edge. Here, the boundary line moves faster and leads to the observed double-S-shape. The collapse dynamics were qualitatively the same for all observed expulsion processes in this experiment. In this experiment the nucleation occurred for all transitions close to the centre of the contact area. In total, four transitions starting from $n = 6$ down to $n = 3$ layers of OMCTS molecules were accessible in this experimental run. From the video images it can be clearly seen, that the spreading of the area with reduced film thickness is getting slower with decreasing film thickness. In order to extract more detailed information, the speed of the boundary line between the regions with thickness n and $n - 1$ was extracted from the images using an image processing program (ImagePro+) and the result is shown in Figures 5.2 and 5.3 and in Table 5.1.

In the following, the experimental results are compared with the theoretical PT-model. Figure 5.2 shows a comparison of the experimental data for the expulsion process from $n = 4 \rightarrow 3$ with kinetic Monte Carlo simulations and analytical results as well. The analytical curve is given by the analytical

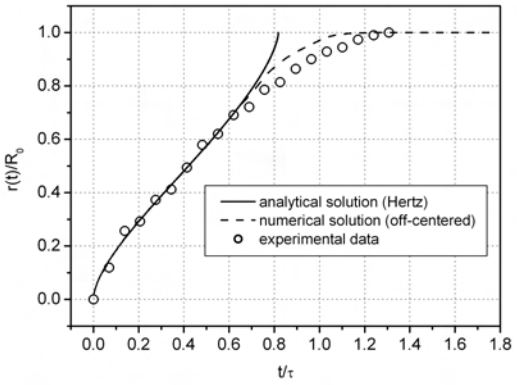

Figure 5.2: A comparison of the experimental data (open circles) for the expulsion process from $n = 4 \rightarrow 3$ with kinetic Monte Carlo simulations (dashed line) and analytical results (solid line).

solution to a centro-symmetric case for a Hertzian pressure distribution (Equation 2.6). Combining Equation 2.14 with 2.6 and introducing reduced units $\tilde{A} = A/A_0$ and $\tilde{t} = t/\tau$ one obtains:

$$\frac{d\tilde{A}}{d\tilde{\tau}} \ln \tilde{A} = -\frac{3}{2}\sqrt{1-\tilde{A}}. \tag{5.1}$$

Integrating Equation 5.1 results finally in the following equation for the analytical curve [57]:

$$\tilde{t} = \frac{4}{3}\left[\sqrt{1-\tilde{A}}(ln\tilde{A} - 2) + ln\left(\frac{1+\sqrt{1-\tilde{A}}}{1-\sqrt{1-\tilde{A}}}\right) + 2 - ln4\right] \tag{5.2}$$

The computer simulations of the squeeze-out process consider both the nucleation at the centre of the contact area and the

Table 5.1: Velocity of the boundary line of subsequent expulsion processes.

expulsion process	$v_{boundary}[\mu\mathrm{m/s}]$
$6 \rightarrow 5$	36.8
$5 \rightarrow 4$	31.8
$4 \rightarrow 3$	14.8
$3 \rightarrow 2$	2.7

off-centred case. In these simulations a kinetic Monte Carlo scheme was used [56], where the time scale is linearly related to the physical time scale. The effective radius in this diagram is defined as $\tilde{r} = \tilde{A}^{1/2}$. The experimental data agree well with the simulation data during most of the squeeze-out process. Furthermore, at the end of the expulsion process, there is also a qualitative agreement with the simulated data for the off-centred case. As already mentioned, the experimental nucleation occurred slightly off-centred. Because the experimental data agree very well with the analytical solution based on theory, it can be concluded, that at least during the expulsion process the OMCTS film is most likely in a two-dimensional liquid-like state. This finding is also confirmed by B.N.J. Persson *et al.* [79].
The dynamics of the boundary line for all observed expulsion processes in this experimental run is compared in the diagram shown in Figure 5.3. In this diagram the radius of the area with (n-1) layers versus time for the expulsion processes from $n = 6 \rightarrow 5$, $n = 5 \rightarrow 4$, $n = 4 \rightarrow 3$ and $n = 3 \rightarrow 2$ is shown. The slope of the plotted data represents the speed of the boundary line. It is found that the average speed decreases with decreasing number of confined layers (see also Table 5.1). Fitting the analytical solution to the experimental data one obtains the effective friction

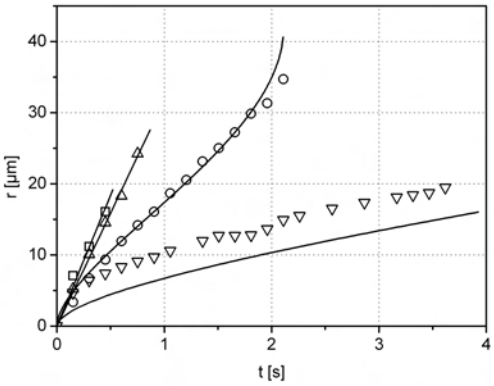

Figure 5.3: Radius of area with reduced film thickness $n-1$ verus time for four consecutive expulsion processes ($n = 6 \rightarrow 5$ (squares), $n = 5 \rightarrow 4$ (triangles up), $n = 4 \rightarrow 3$ (circles), and $n = 3 \rightarrow 2$ (triangles down)). The solid lines represent the theoretical fitting curves. The deviation of the transition $n = 3 \rightarrow 2$ is related to a violation of the circular symmetry assumed for the analytical curve.

coefficient η_{eff} for each layer expulsion, respectively. The analytical fits are shown as solid lines in Figure 5.3. Due to the limited acquisition rate of the camera it was not possible to record enough images for the two fast layer expulsions to perform an appropriate fitting of the data. Furthermore both transitions, $6 \rightarrow 5$ and $5 \rightarrow 4$ nucleated in the centre of the contact area. Hence, the velocity of the boundary was determined by performing a linear fit. The deviation between the analytical solution and the experimental data for the slowest expulsion process shown in Figure 5.3 is attributed to deviations from the circular symmetry assumed for the analytical curve. Alternatively to fitting Equation 2.14 to the

experimental data the effective friction coefficient η_{eff} can be determined by measuring the total time of a single layer expulsion and using Equation 2.16. This is possible because η_{eff} is the only adjustable parameter in Equation 2.16 and this allows for a easier and faster analysis of the data.

5.1.2. Effective friction dependence on film thickness

From the data displayed in Figure 5.3 the effective friction coefficient has been determined, and in Figure 5.4 is plotted against the film thickness in units of molecular layers. The

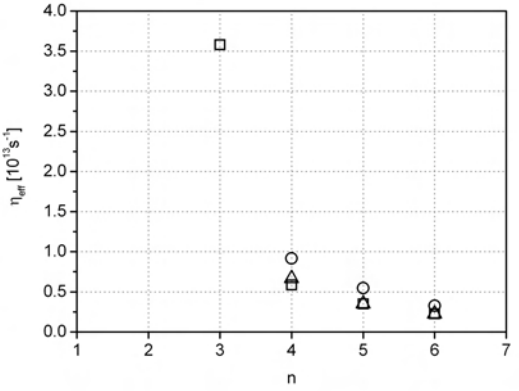

Figure 5.4: The effective friction coefficient η_{eff} versus OMCTS film thickness in units of the molecular diameter. The different symbols refer to different experimental runs on the same set of samples.

diagram in Figure 5.4 thus shows the effective friction coef-

ficient $\eta_{eff}(n)$ of the n-th layer during the layer expulsion $n \rightarrow n-1$. It can be seen clearly that η_{eff} increases with decreasing number of confined OMCTS layers. For all runs in this experiment similar values of η_{eff} for the respective film thicknesses were obtained. Unfortunately, it was only possible to record one image sequence for the expulsion process $n = 3 \rightarrow 2$ in this experiment. Obviously, the increase of the friction coefficient corresponds to the decreasing velocity of the boundary line between the n and $n-1$ area. It should be pointed out here, that $\eta_{eff}(3)$ is larger than $\eta_{eff}(6)$ by a factor of approximately ten.
Further experiments with re-cleaved mica samples and OMCTS have been performed and yielded similar results for the effective friction coefficient η_{eff}. Figure 5.5 illustrates the set of values obtained for η_{eff} versus film thickness for two further experiments with different mica substrates. Both experiments shown in Figure 5.5 were performed under similar conditions, where the only difference was in the thickness of the mica substrates ($d_{mica,total}$ in (b) is thicker than in (a)). In both cases the applied load rates were varied in a certain range such that, for all measurements presented in Figure 5.5, the nucleation of the expulsion processes occurred close to the centre[1]. In the case of the thicker substrates no dependence of the effective friction coefficient on the different approach rates ($0.2 \ldots 6.4$ mN/s) was found. For the thinner of the two substrates load rates in the range $0.08 \ldots 1.9$ mN/s were applied. Here, for the highest load rate (open stars in Figure 5.5(a)) the values determined for the effective friction coefficient are significantly larger than for smaller load rates. The layer expulsion $n = 2 \rightarrow 1$ was accessible in only one of the presented experiments (Figure 5.5(b)). The effective friction coefficient determined from this transition is $\eta_{eff} = 21.4 \times 10^{13}$ s^{-1}. The significance of this value will

[1] Different expulsion scenarios related to higher approach rates will be discussed in Section 5.2 and 5.3

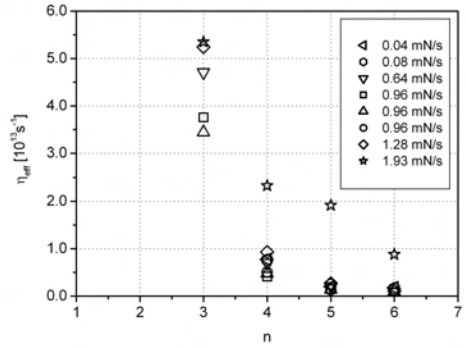

(a)

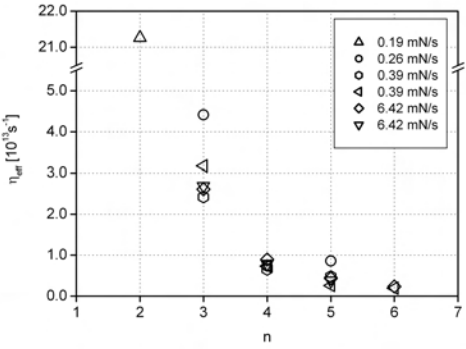

(b)

Figure 5.5: Effective friction coefficient η_{eff} for two experiments with different samples (Both experiments were performed at room temperature). The experimental parameters of the samples are: (a) $d_{Mica,total} = 1.8155$ μm, $A = 32.9\%$, and (b) $d_{Mica,total} = 2.9965$ μm, $A = 48.6\%$. Different symbols in the plots refer to different experimental runs with different applied load rates. The deviation of the values represented with open stars in (a) can be related to a quite fast increase of the applied load.

be discussed later in this chapter.

5.1.3. The extended hydrodynamic model

In order to understand the increase of the effective friction coefficient with decreasing number of confined molecular layers, the situation is now considered on a microscopic level. During an expulsion process (illustrated for a transition from $n = 4 \rightarrow 3$ layers in Figure 5.6), one finds three different processes involving the dynamics.

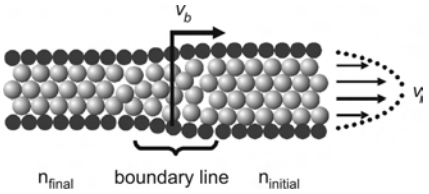

Figure 5.6: Schematics of the expulsion process $n = 4 \rightarrow 3$.

(i) At the leading edge of the boundary zone, the well defined layer structure (thickness n) disappears and the film becomes disordered.

(ii) Behind the regime of the boundary line, the liquid molecules change from the disordered structure into a well defined layered structure with thickness n_{final}.

(iii) Due to mass conservation, the material in the regime of thickness $n_{initial}$, ahead of the boundary line, flows towards the edge of the contact area into the bulk liquid. In contrast, the material in the area with n_{final} is at rest.

All the processes mentioned contribute to the dissipation of energy during a expulsion process. Whereas processes (i) and (ii) are related only to the one dimensional boundary line, the last process involves the transport of molecules everywhere in the much larger two dimensional regime with thickness $n_{initial}$ in the contact area. Therefore the third process is assumed to dominate the dissipation.
To describe the situation for a system consisting of N layers mathematically, the hydrodynamic model by Persson and Tosatti is extended to a system consisting of N liquid layers. The liquid layers in the system are assumed to be independent from each other. Each layer i moves with a velocity v_i, which is different from layer to layer. Because the liquid layers are regarded as independent, two different drag coefficients η_{ll} and η_{ls} are introduced. The liquid-liquid friction coefficient η_{ll} arises from the sliding of two adjacent liquid layers on top of each other. The liquid-solid friction coefficient η_{ls} takes into account the interaction between a liquid layer and a solid wall. This is the case for the top and the bottom layer of the system, where each interacts on one side with the mica substrate. Thus we can write,

$$\eta_{1,0} = \eta_{N,N+1} = \eta_{ls} \tag{5.3}$$

$$\eta_{i,i-1} = \eta_{i,i+1} = \eta_{ll} \qquad (i = 1 \ldots N) \tag{5.4}$$

Furthermore, we assume that the two-dimensional pressure $p_{2\mathrm{D}}$ is distributed evenly between all layers. The stress acting on each layer is thus given by $p'_{2\mathrm{D}} = p_{2\mathrm{D}}/N$. The velocity v_i

for layer i is then determined by:

$$\begin{aligned}
\nabla p'_{2D,n=1} &= \rho_{2D}[\eta_{ls} v_1 + \eta_{ll}(v_1 - v_2)] \\
\nabla p'_{2D,n=2} &= \rho_{2D}[\eta_{ll}(v_2 - v_1) + \eta_{ll}(v_2 - v_3)] \\
&\vdots \\
\nabla p'_{2D,n=i} &= \rho_{2D}[\eta_{ll}(2v_i - v_{i-1} - v_{i+1})] \\
&\vdots \\
\nabla p'_{2D,n=N} &= \rho_{2D}[\eta_{ll}(v_N - v_{N-1}) + \eta_{ls} v_N]
\end{aligned} \tag{5.5}$$

Writing this set of equations as a matrix and introducing $B = \eta_{ls}/\eta_{ll}$ one obtains:

$$\begin{pmatrix}
1+B & -1 & 0 & \cdots & 0 \\
-1 & 2 & -1 & 0 & \vdots \\
0 & -1 & 2 & -1 & \vdots \\
\vdots & & & \ddots & -1 \\
0 & \cdots & \cdots & -1 & 1+B
\end{pmatrix}
\begin{pmatrix}
v_1 \\ v_2 \\ \vdots \\ \vdots \\ v_N
\end{pmatrix}
= \frac{\nabla p'_{2D}}{\eta_{ll}} \cdot \underline{\mathbf{1}} \tag{5.6}$$

Now this system can be solved easily for the velocities v_i of each layer for a fixed ratio B. In the experiments presented here, the velocity v_b of the boundary line is the accessible quantity. The schematic illustration in Figure 5.7 shows how mass conservation implies that this velocity must be given by

$$v_b = \sum_{i=1}^{N} v_i. \tag{5.7}$$

As theoretically expected from a Poiseuille flow, the velocities v_i of the single layers follow a parabolic profile. With Equation 5.7 the effective friction coefficient η_{eff} can be obtained from

$$\nabla p'_{2D} = \rho_{2D} \eta_{eff} v_b. \tag{5.8}$$

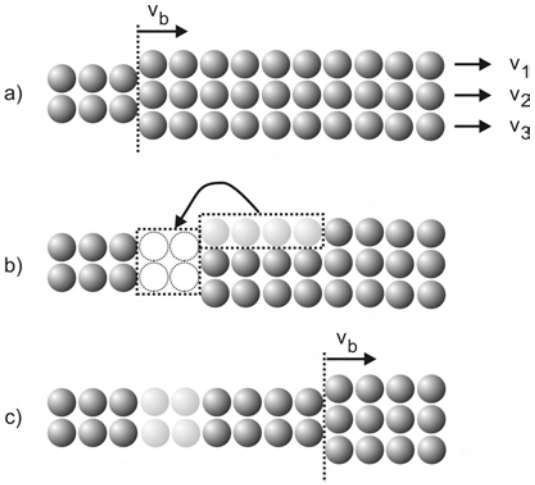

Figure 5.7: This illustration demonstrates that the velocity of the boundary line is given by the sum of the velocities of the single layers. For simplicity a velocity of two molecular diameters per second for all layers is assumed. The developed "holes" in (b) (illustrated with dashed circles) are filled with the light gray molecules.

Thus, one finds the following implicit function of both friction coefficients η_{ll} and η_{ls}:

$$\eta_{eff}(n) = \left| \frac{\nabla p_{2D}}{\rho_{2D} \sum_i v_i} \right| \tag{5.9}$$

In order to obtain best fit values for both friction coefficients, this model was fitted to the experimental data. Here, the mean square deviation χ^2 between the model function and the experimental data was calculated. This fitting routine works as follows. First, the velocity profile for the number of confined layers corresponding to the measured value of the effective friction coefficient is calculated with η_{ls} and η_{ll}

as parameters. From the calculated velocities of the single layers one obtains the velocity of the boundary line and thus a value $\eta_{eff,calculated}(n, \eta_{ls}, \eta_{ll})$ depending on the number of layers and the two friction coefficients. The result of this calculation is represented in a two-dimensional plot of $1/\chi^2$, where χ is given by

$$\chi = \eta_{eff,calculated}(n, \eta_{ls}, \eta_{ll}) - \eta_{eff,experiment}(n). \quad (5.10)$$

The maximum of $1/\chi^2$ yields the best fit values for the coefficients η_{ls} and η_{ll}, and the degree of correlation is indicated by the shade of the grey level with the lightest grey representing the maximum of $1/\chi^2$. Figure 5.8 shows the results of the fitting routine for the three sets of experimental data for $\eta_{eff}(n)$ presented above. In Figure 5.8(a)-(c) only the experimental values for the expulsion processes down to $n = 3 \rightarrow 2$ are included. The experimental data correspond to the values of η_{eff} shown in Figure 5.4 and 5.5, respectively. From these plots it is possible to estimate a value for η_{ll}. Within the margin of error, obtained from the full width at half maximum of the $1/\chi^2$-plot, these values agree for the different experiments. As can be seen clearly, the liquid-solid friction coefficient η_{ls} cannot be determined definitely as it is also necessary to know a value for the effective friction coefficient for $n = 2$. Including $\eta_{eff}(n = 2)$ results in the plot shown in Figure 5.8(d). Thus, for the friction coefficients one obtains the following values

$$\begin{aligned} \eta_{ll} = &\quad (0.60 \pm 0.20) \cdot 10^{13}\ \mathrm{s}^{-1} \\ \eta_{ls} = &\quad (21.26 \pm 1.98) \cdot 10^{13}\ \mathrm{s}^{-1} \quad . \end{aligned}$$

From the values obtained the velocity profile across a film with a given thickness can be calculated. Using the values above the ratio of the both friction coefficients is found to be

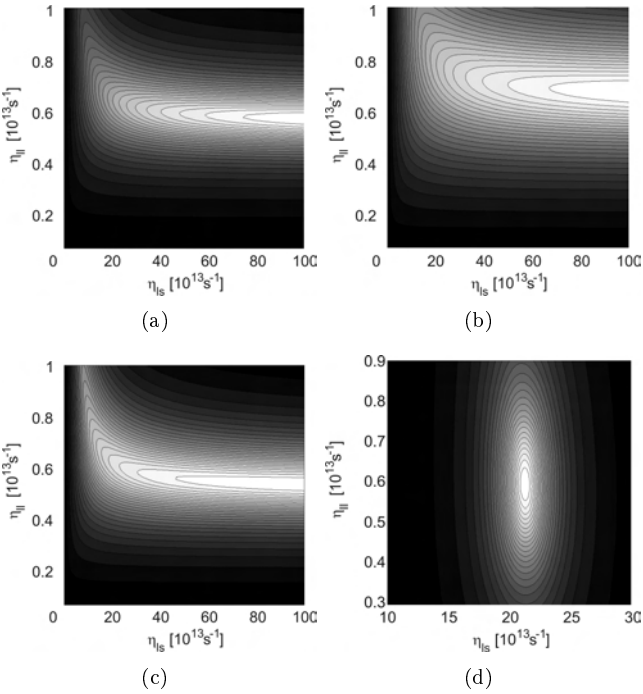

Figure 5.8: Two-dimensional plots of the results of the fitting routine to find values for η_{ll} and η_{ls}. (a)-(c): $1/\chi^2$ for experimental $\eta_{eff}(n)$ down to $n = 3$. (a) represents $1/\chi^2$ for the data shown in Figure 5.4 ($\eta_{ll} = (0.55 \pm 0.13) \cdot 10^{13}$ s^{-1}), (b) for the data shown in Figure 5.5a) ($\eta_{ll} = (0.65 \pm 0.23) \cdot 10^{13}$ s^{-1}) and (c) for the data shown in Figure 5.5b) ($\eta_{ll} = (0.51 \pm 0.14) \cdot 10^{13}$ s^{-1}). Image (d) shows the result of the fitting routine including the experimental value for $\eta_{eff}(2)$.

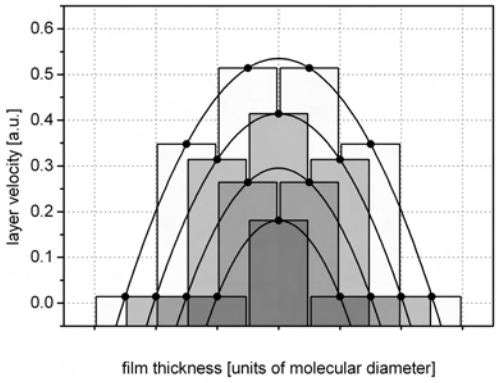

Figure 5.9: Calculated velocity of the single layers for a system consisting of N=6, 5, 4 and 3 layers. The bars indicate the liquid layers.

$B = 35.43$. Figure 5.9 shows the calculated velocity profile for N=6 layers. In this diagram the velocity of the layers is plotted against the film thickness in units of molecular diameters.
It is now possible to determine the slip length b of the flow of the liquid layers. The slip length is defined as [80]

$$b = v / \left(\frac{\mathrm{d}v}{\mathrm{d}z} \right)_0 . \tag{5.11}$$

For large film thicknesses ($N \gg 1$) the discrete profile approaches the analytical hydrodynamic solution for a Poiseuille flow, which can be written as:

$$v(z) = \frac{(d/2)^2 - z^2}{2\eta} \nabla p + v_{slip} \tag{5.12}$$

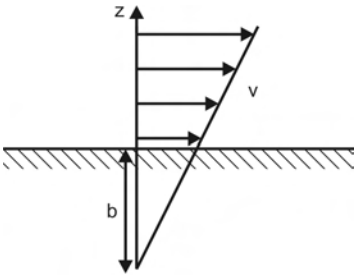

Figure 5.10: Velocity profile of a fluid flow near a solid surface to illustrate the slip length b.

where η is the bulk viscosity, d is the film thickness, $v_{slip} = v_1 = v_N$ is the slip velocity and z is the coordinate perpendicular to the surfaces. It follows from Equation 5.6 that

$$v_{slip} = \frac{\nabla p'_{2D}}{2\eta_{ls}}, \tag{5.13}$$

i.e. the slip velocity vanishes as expected for an increasing liquid-solid friction coefficient $\eta_{ls} \to \infty$. To obtain a value for the slip length, the calculated velocity profile is extrapolated to velocity $v = 0$. From this we obtain, that the slip length b is smaller than the molecular diameter ($b \approx 0.033 \cdot d_{OMCTS}$) and that therefore the slip is negligible for the present parameters. Furthermore the experimental data can be compared with the model function as shown in Figure 5.11. It can be clearly seen that the experimental and the model data are in good agreement. Figure 5.11 also displays the flow resistance of a thin liquid film calculated in the hydrodynamic limit (dashed line). For the model presented η_{ll} does not depend on the number n of layers confined between the mica substrates. This means that the effective friction coefficient $\eta_{eff}(n)$ should converge towards the flow resistance $\eta(d)$ calculated in the hydrodynamic limit for large film thicknesses

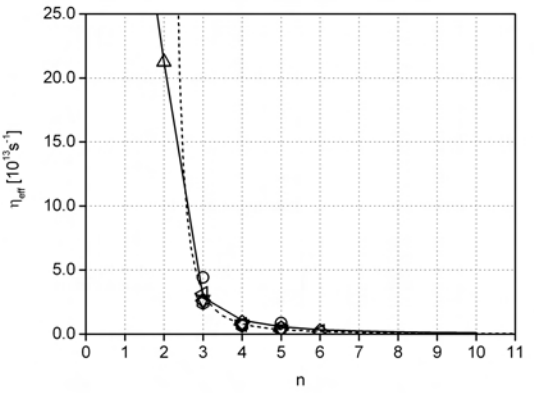

Figure 5.11: Comparison of the experimental $\eta_{eff}(n)$ from Figure 5.5b) with the model function (solid line) calculated for $\eta_{ll} = 0.60 \cdot 10^{13}$ s^{-1} and $\eta_{ls} = 21.26 \cdot 10^{13}$ s^{-1}. The hydrodynamic limit (dashed line) is shifted by two molecular diameters to the right, because the two outer layers can be regarded as immobile.

$(n \to \infty)$ where the flow resistance is given by:

$$\eta(d) = \frac{12\eta_{bulk}}{\rho d^2}. \tag{5.14}$$

One obtains $\eta_{ll,hydro} = \eta_{bulk}/(\rho_{2D} d_0) = 0.3 \cdot 10^{13}$ s^{-1} in this limit, which is reasonably close to the best fit value for η_{ll}. Adjacent liquid layers with well ordered molecules thus exhibit a momentum transfer that is close to the situation found for sliding between equivalent layers of disordered bulk liquid. These results are in qualitative agreement with non-equilibrium molecular dynamics simulations [81,82]. As shown above, the two outer layers can be regarded to be stagnant. This leads to a shift of the hydrodynamic limit (dashed line

in Figure 5.11) by n=2 to the right compared to a situation with mobile outer layers. The hydrodynamic limit is then in agreement with the experimental data and it is thus reasonable to accept the findings of the model presented. In contrast to a $1/d^3$-dependence of the effective friction coefficient, as would be expected from a simple Poiseuille flow, a $1/d^2$-dependence is obtained. The reason for this relates to the two-dimensional nature of the model and the even distribution of the pressure on the layers. The origin of the increase of $\eta_{eff}(n)$ with decreasing film thickness compared to the extrapolated bulk behaviour is the increasing weight of η_{ls} compared to η_{ll} with decreasing n. As can be seen in Figure 5.8 the determination of η_{ll} is not dependent on whether the minimum value for the number of confined layers is $n = 1$ or $n = 2$. In both cases η_{ll} is of the same order of magnitude as the value $\eta_{ll,hydro}$ calculated in the hydrodynamic limit. On the other hand, η_{ls} is determined by the experimental value of the friction coefficient for the expulsion process $n = 2 \rightarrow 1$. However, η_{ls} is so large that the first layer can be regarded as immobile.

5.2. Thin substrates

5.2.1. Elastohydrodynamics

Using the re-cleaving step for the preparation of the mica samples it is possible to obtain very thin substrates with a total thickness smaller than 1 μm. Experiments with these thin mica sheets exhibit a strong dependence of the collapse dynamics on the applied load rate. For rather small load rates below a critical value (< 4 mNs^{-1} for the current set of samples), qualitatively similar behaviour of the collapse dynamics as for thicker samples (Section 5.1) are observed.

But in the case of the thinner substrates, the expulsion of only one liquid layer was observed. This may be explained by a reduction of activation barriers for soft substrates, which prevents the observation of layer expulsions at higher n. Completely different expulsion dynamics were found for load rates above the critical value. Figure 5.12 displays this behaviour in a series of snapshots for high approach rates. For the

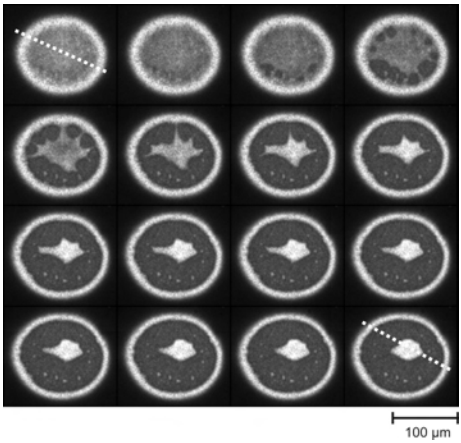

Figure 5.12: Snapshots from an experiment with very thin substrates at a stepwise approach from 0 to 15 mN. The incident light is adjusted in a way such that brighter gray level corresponds to larger film thickness. The time difference between subsequent images is $\Delta t = 300$ ms. The dotted lines in the first and the last images indicate the positions of the cross-sections shown in Figures 5.13 and 5.14, respectively.

images presented the wavelength of the incident light was adjusted to the right side of a transmission peak. Thus a darker gray level corresponds to reduced film thickness. The load was increased stepwise from 0 to 15 mN. The nucleation

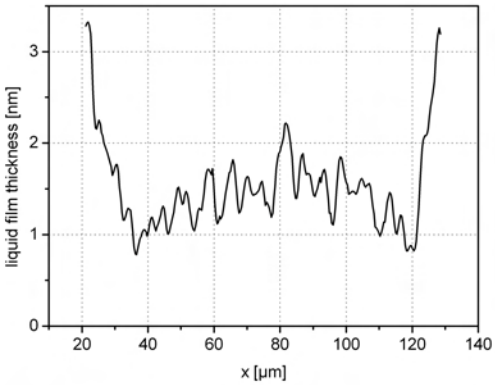

Figure 5.13: Liquid film profile from the first image in Figure 5.12. Due to the additional pressure exerted from the liquid onto the substrates, the substrates are bent outwards. The nucleation of holes in the liquid layer will occur at the edge of the contact area, where the separation between the mica surfaces is the smallest.

does not occur close to the centre of the contact area, but at several spots at the edge of the contact region. This can be seen in the first row of Figure 5.12. The dark spots along the edge of the contact area correspond to a direct mica-mica contact. The scenario can be explained via an elastohydrodynamic deformation of the mica substrates. It was already shown in Section 2.2.3 (Equation 2.4) that due to the finite viscosity of the fluid, the liquid exerts an additional pressure on the substrates when they are brought together with a fast approach rate. This leads to an outward bending of the mica substrates. Figure 5.13 shows a cross-section through the contact area in the initial state of the approach. The thick-

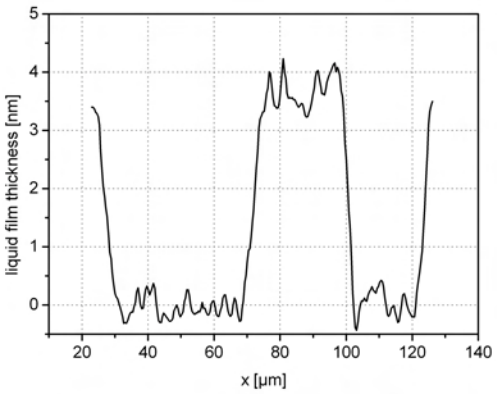

Figure 5.14: Cross-section through the last image in figure 5.12. The flat top of the trapped droplet and its sharp edges are a remarkable result. The height of (3.7±0.1) nm is in good agreement with four discrete layers of OMCTS molecules.

ness of the liquid film is clearly larger in the centre of the contact area than at the edge. The nucleation will occur at the edge of the contact area where the surfaces are the closest together. While these islands of reduced film thickness grow, more nuclei continue to appear at the edge and the areas of direct mica-mica contact merge. Consequently, a part of the liquid in the contact zone is expelled into the bulk liquid around the contact area. The rest of the liquid within the contact area is trapped and shrinks to a single patch. With time, this patch shrinks laterally under the condition of mass conservation. During the shrinkage a brighter rim around the edge of the liquid patch can be seen (see the first two images in the second row of Figure 5.12). Similar observations have been made in experiments on the dewetting of silicon oil films

between hard silicon and soft polymeric surfaces [48] or during dewetting of thin polymer films on solid substrates [83]. A few seconds later in the experiment, the patch has transformed into a nearly circular droplet. This droplet is brighter than the initial film, i.e. thicker. The shape of the droplet is remarkable, with sharp edges and a flat top as shown in the cross-section in Figure 5.14. The droplet adopts this cylindrical shape, because it still feels the presence of the oscillatory interface potential. The height of the trapped droplet is approximately 3.7 nm, which corresponds to four monolayers of OMCTS molecules. The process of shrinkage and increase of the thickness are related to the elastic properties of the substrates. As soon as the trapped liquid is separated from the edge of the contact area, it tends to minimise its energy and conserves its mass. The energy of the droplet can be approximated with [6]:

$$U(\rho, h) = 2\gamma\pi\rho^2 + \frac{E}{2(1-\nu^2)}\rho h^2 \tag{5.15}$$

where E is the elastic modulus and ν is the Poisson ratio of mica. During the shrinkage, the interface free energy changes as a result of changes in the interfacial area. This is represented by the first term in Equation 5.15. The second term describes the elastic energy of the work required to press a rigid disc of radius ρ and height h by $h/2$ into two semi-infinite elastic substrates on each side [84]. The lateral size of the droplet is in the range of a few micrometers and thus it is reasonable to neglect the contribution of the line tension. In order to minimise $U(\rho, h)$ the liquid patch saves interfacial energy by laterally shrinking and increasing thickness at the expense of elastic energy. The diagram in Figure 5.15 shows the energy of the trapped liquid droplet calculated from Equation 5.15 under the condition of mass conservation. The equilibrium height of the droplet can be estimated with the values $\nu = 0.44$, $\gamma = 1$ mJ/m^2. The elastic mod-

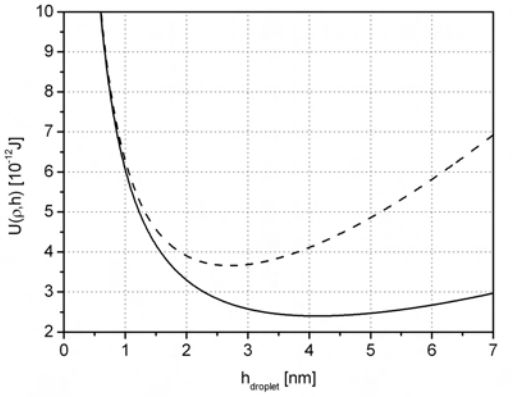

Figure 5.15: Energy of a liquid droplet trapped in the contact area. Under the condition of constant droplet volume one obtains from the minimum of $U(\rho, h)$ the equilibrium shape of the droplet. The dashed line represents $U(\rho, h)$ calculated with $E_{\text{mica}} = 1.72 \cdot 10^{10}$ N/m^2; the solid line is calculated for $E_{\text{eff}} = 6.0 \cdot 10^9$ N/m^2 as obtained from the experiment.

ulus for mica is $E_{\text{mica}} = 1.72 \cdot 10^{10}$ N/m^2 [64]. Using the values above one obtains for the cylindrically shaped droplet an equilibrium height of $h \approx 2.7$ nm. This is in contrast to the measured of the droplet. The deviation of this calculation to the measured height of the droplet is related to the elasticity of the substrate used. For a more realistic description of the problem one has to take into account, that the mica is glued with a relatively thick layer of epoxy glue onto the sample support. In this experiment the mica samples are very thin and thus the underlying glue layer contributes to the elasticity of the sample. The result is an effective elastic modulus E_{eff} of the mica sample together with the glue

layer. This effective elastic modulus can be estimated from separate experiments, where the applied load dependence of the radius of the contact area for a dry contact is measured. The contact radius for an adhesive contact is given by the theory of Johnson, Kendal and Roberts (JKR) [85]

$$R_{contact}^3 = \frac{R}{E}(F + 6\pi\gamma R + \sqrt{12\pi\gamma RF + (6\pi\gamma R)^2}), \quad (5.16)$$

where $R_{contact}$ is the radius of the contact area, R the radius of the curved sample, F the applied force, γ the interfacial energy and E the elastic modulus of the sample. With this, we can estimate the value for the effective elastic modulus to approximately $6.0 \cdot 10^9$ N/m^2 (see Figure 5.16). This agrees

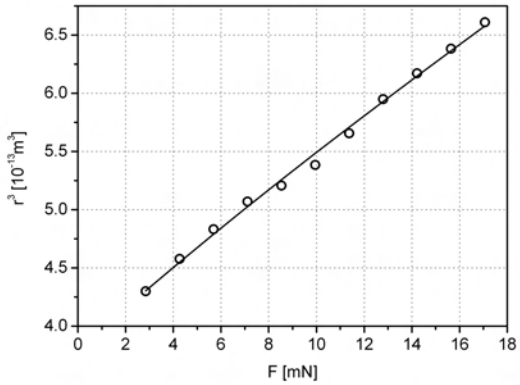

Figure 5.16: Plot of the third power of the radius of the contact area against the force. The solid line represents the represents the JKR fitting curve (Fitting parameters: $E = 6.0 \cdot 10^9$ N/m^2, $R = 5.57$ cm and $\gamma = 19$ mJ).

with the findings of Horn *et al.*, who report on effective elasticities of mica sheets glued on a silica lens in the range of

$3 \cdot 10^9 \ldots 2 \cdot 10^{10}$ N/m^2 [86]. The best fit parameter for the radius of curvature is in good agreement with the radius of curvature of 5 cm of the sample holder. Only the value for the surface energy of the mica deviates significantly from the literature value of $\gamma = 120$ mJ/m^2. Calculating the energy of the trapped droplet with this value for E_{eff} we find an equilibrium droplet shape with a height of 4.1 nm, which agrees reasonably with the measured height. For a precise determination of the shape of the droplet with Equation 5.15 it is necessary to know exactly the elastic modulus and the interfacial energy, which has not been given for the experiment presented here.

5.2.2. Dynamics of trapped droplets

In general larger droplets trapped inside the contact area are unstable and do not remain in the same place. In the present experiment the droplet was found to be expelled from the contact area with time. The shape and the volume of the droplet were conserved until the droplet reached the edge of the contact area. Figure 5.17 shows the motion of the trapped droplet. Inside the contact zone the pressure distribution is not homogeneous, but has a maximum in the centre. For example it can be given by a Hertzian pressure distribution (Equation 2.6). The droplet shown in Figure 5.17 is slightly off-centred and thus a different pressure acts on each point of its boundary. Integrating along the droplets boundary yields a resulting force. This force is directed towards the edge of the contact zone and pushes the droplet out of the contact region [17]. From the recorded videos it can be found that the boundary line of the droplet seems to get pinned from time to time. The pinning is only transient and the droplet continues to move after a short while. As it approaches the edge of the contact area it starts to elongate and to form a

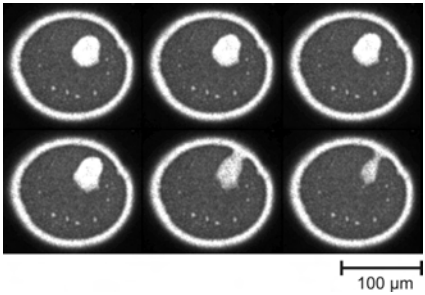

Figure 5.17: Snapshots of the trapped droplet with $n = 4$ layers of OMCTS. Due to the pressure distribution within the contact area with a maximum in the centre a net force exerted on the droplet pushes it towards the edge of the contact region. Time between the images: $\Delta t = 250$ ms.

liquid neck. Most of the material flows out of the contact region into the surrounding reservoir through this neck. In the final state, a small amount of liquid remains inside the contact area. Some smaller droplets, that were trapped in the contact region as well, remained stationary after their formation.
The motion of the droplet can be described in terms of hydrodynamics [17]. The elastic energy of the substrates at a trapped droplet with an applied three dimensional pressure $P(\vec{x})$ is given by

$$U = \int dx^2 P(\vec{x}) h(\vec{x}). \tag{5.17}$$

With the assumption that the shape of the droplet is not changed with varying position in the contact area one obtains the force acting on the droplet by integrating along the

boundary line s of the droplet with height h_0:

$$\vec{F} = -\frac{\partial U}{\partial \vec{r}} = -\oint \mathrm{d}s h_0 P(\vec{r} + \vec{x}_s)\vec{n}_s. \tag{5.18}$$

in this equation, $\vec{r}$ is the position of the centre of mass of the droplet, $\vec{x}_s$ is the position of the boundary line relative to the centre of mass and $\vec{n}_s$ is the normal vector to the boundary line directed away from the droplet. With this one finds, that the forces acting on the trapped droplets are of the order of $10^{-8} \ldots 10^{-7}$ N. The typical shear stress, that is calculated by dividing by the droplet area is thus smaller than 1 kPa. If the droplet is small enough the energy stored in the substrates can be approximated by

$$U = \int d^2x P(\vec{x})h(\vec{x}) \approx P(\vec{r}) \int d^2x h(\vec{x}) = P(\vec{r})\Delta V, \tag{5.19}$$

where ΔV is the volume of the droplet. Assuming that the pressure $P(\vec{r})$ is only dependent on the distance $r = |\vec{r}|$ from the centre of the contact area results in a force $F(r) = -P'(r)\Delta V$ acting in radial direction. Consider now a droplet with area ΔA and height h_0 ($\Delta A \ll A_{\mathrm{contactarea}}$). The velocity $v(r)$ of the droplet can be extracted from the video snapshots. Presuming an overdamped motion one can neglect the inertial force acting on the island. Thus the force $F(r)$ must just balance the frictional drag force from the solid walls:

$$\rho_{2D}\Delta A\overline{\eta}v(r) = F(r) \tag{5.20}$$

Assuming a Hertzian pressure profile (Equation 2.6) the force acting on the droplet can be determined for all positions of the droplet in the contact area. From Equation 5.20, and including the experimental data for ΔA and $v(r)$, values for the friction coefficient $\overline{\eta}$ were found to be in the range of $(2..4)\cdot 10^{13}$ s^{-1}, which are in agreement with the values found for the effective friction coefficient for 4 layers (Section 5.1.2).

In the following, experiments with thick substrates and high approach rates are shown, where the nucleation also occurs at the the edge of the contact area for the first expulsion processes.

5.3. Stiff substrates and high approach rates - a mixed scenario

As it was shown in the previous sections, the expulsion dynamics of single liquid layers out of the contact region depends on one hand on the substrate elasticity and on the other hand on the approach rate. In the case of slow approaches on thick and thus stiffer substrates, the expulsion process started at holes that nucleated close to the centre of the contact area. For slow approaches and soft substrates the same scenario was observed. For fast approaches the nucleation occurred at several spots at the edge of the contact zone. In the following, the expulsion dynamics of liquid layers confined between thick substrates will be discussed for the case of a fast approach.
Figure 5.18 shows the snapshots of the transitions starting from $n = 5$ down to $n = 2$ layers for a fast load ramp. The snapshots show nicely that in the case of a fast approach applied to stiffer substrates one obtains a kind of a mixed scenario. In the beginning the dynamics are qualitatively similar to fast approaches on thin substrates. Darker spots, corresponding to reduced film thickness, appear at the edge of the contact area. These areas grow and merge with time. The bright area shrinks and finally vanishes in the centre of the contact area, which means that the volume of the bright island is not conserved. In contrast to the situation described in section 5.2, the liquid patch does not transform into a droplet trapped within the contact area but instead the

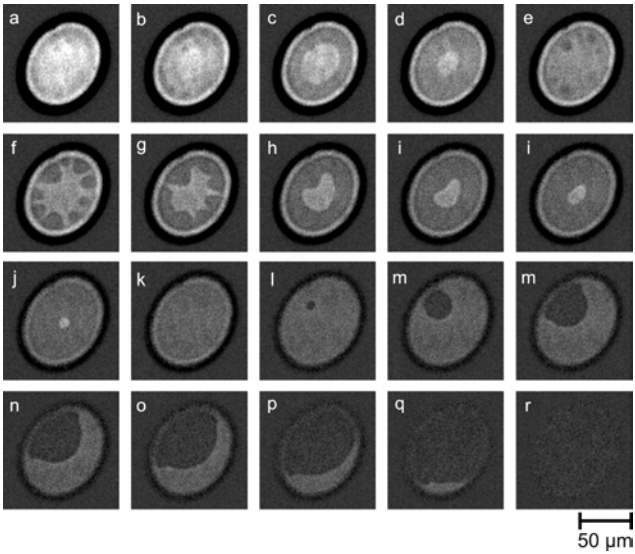

Figure 5.18: Snapshots of a fast approach applied to stiff substrates. The images show the transitions from $n = 5 \rightarrow 4$ (a-d), $n = 4 \rightarrow 3$ (e-j) and $n = 3 \rightarrow 2$ (l-r). The incident light is adjusted in a way such that a brighter gray level corresponds to larger liquid film thickness. In the beginning the nucleation starts at several places at the edge of the contact area and the liquid layer shrinks to a patch in the centre of the contact area and disappears. The last observed layer expulsion exhibits similar dynamics as for a slow approach. Time between images: a-l: $\Delta t = 100$ ms, m-t: $\Delta t = 200$ ms.

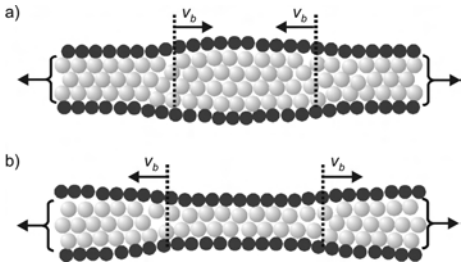

Figure 5.19: Schematics of the expulsion process $n = 4 \rightarrow 3$ (a) and $n = 3 \rightarrow 2$ (b) for a fast approach applied to thick substrates. Whereas in (a) the boundary line move inwards with the velocity v_b due to elastohydrodynamic deformation of the substrates, it moves to the edge of the contact area in (b). In both cases the dissipation takes place in the region of $n = 3$ layers.

liquid molecules are pushed into adjacent liquid layers and after that squeezed out of the contact zone. In the beginning the dynamics can be described again in terms of an elastohydrodynamic behaviour. Initially the mica substrates are bent outwards due to the additional pressure exerted by the liquid. Here, the boundary line between the areas with different film thicknesses moves inwards (transitions $n = 5 \rightarrow 4$ and $n = 4 \rightarrow 3$). After the mica has relaxed the behaviour changes to the case with nucleation close to the centre of the contact area. Then, the last observed layer expulsion in this experimental run ($n = 3 \rightarrow 2$), spreads towards the edge of the contact region (see Figure 5.19). Assuming that Figure 5.19 describes the situation qualitatively correctly, in both transitions, $n = 4 \rightarrow 3$ and $n = 3 \rightarrow 2$ the dissipation in the system should take place in the region between the edge of the contact area and the moving boundary line. Here, the thickness is in both cases $n = 3$ layers. Initial investigations were made on the velocity of the boundary line for the tran-

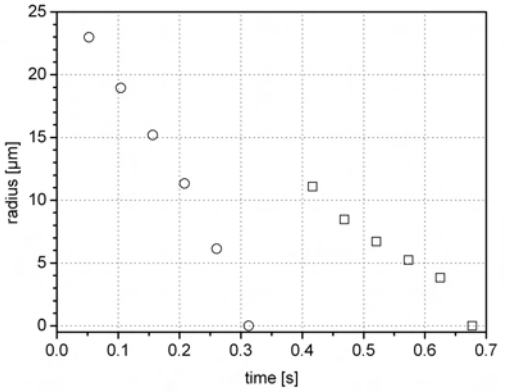

Figure 5.20: Plot of the radius of the bright island in Figure 5.18 against time for the film thickness transitions $n = 5 \rightarrow 4$ (circles) and $n = 4 \rightarrow 3$ (squares). Both transitions start at the time t=0 s, but the data points are only taken from images with an approximately circular bright island.

sitions $n = 5 \rightarrow 4$ and $n = 4 \rightarrow 3$ (see Figure 5.18). Figure 5.20 shows a plot of the radius of the bright island versus the time of the expulsion process. The data were taken from video snapshots, where the shape of the island was approximately circular. As expected the velocity v_b of the boundary line decreases for decreasing film thickness. Calculating values for the effective friction coefficient from v_b, one obtains $\eta_{eff} = 4.2 \cdot 10^{10}$ s^{-1} ($n = 5 \rightarrow 4$) and $\eta_{eff} = 1.84 \cdot 10^{11}$ s^{-1} ($n = 4 \rightarrow 3$). These values are significantly smaller compared to the results obtained in Section 5.1.2. This is possibly related to more complicated processes of the expulsion than assumed above. For further detailed investigations of the complete scenario the PT-model cannot be used. In order to

obtain more information, a model needs to be developed to describe the experimental observations presented here.

5.4. Further remarks on dynamical SFA experiments

5.4.1. Summarised findings of the dynamical processes

In this work the dynamics of the expulsion processes of thin liquid films of the model lubricant OMCTS have been investigated. It was found that the drainage scenario depends on the thickness, and thus the elasticity of the samples, and on the applied load rates.
For thick and thin mica substrates with low approach rates the dynamics of the roughly circular boundary line the dynamics are in good agreement with the simple hydrodynamic PT model, if the nucleation of the expulsion processes occurs in the centre of the contact region. For off-centred nucleation the dynamics can be described quantitatively with numerical simulations [57]. Furthermore the effective friction coefficient was determined depending on the film thickness. The sensitivity of the two-dimensional imaging technique in terms of effective viscosity is about two orders of magnitude better than the highest reported resolution in shear force measurements [11]. It is a remarkable result of the experiments that the effective friction coefficient increases by roughly one order of magnitude compared to the bulk when the film thickness decreases to n=3. This is in contrast to experiments on OMCTS confined between mica surfaces performed by other groups [11, 12, 14, 15, 87, 88] that reported an increase in the viscosity by several orders of magnitude within roughly

the same range of film thickness. They concluded that the thin liquid films solidify under confinement. Whilst it is conceivable that the liquid films may solidify under equilibrium conditions, it should also be noted that these earlier experiments were performed with samples prepared in the standard procedure without the re-cleaving step. In more recent experiments by others [71–73], where contamination free surfaces are assured, this increase in the effective viscosity by several orders of magnitude could not be reproduced.
In order to explain the increase in effective viscosity with decreasing film thickness a model was developed including two different friction coefficients. A liquid-solid friction coefficient taking into account the interaction between a liquid layer and a solid wall and a liquid-liquid friction coefficient arising from the sliding of two adjacent liquid layers on top of each other. The model is found to be consistent with the experimental data and the origin of the increase of the effective viscosity with decreasing film thickness is attributed to the increasing weight of the liquid-solid coefficient with decreasing film thickness.
In the case of a fast approach rate applied to thin mica samples the formation of trapped liquid droplets in the contact area was observed. This behaviour can be understood in terms of elastohydrodynamic deformation of the soft substrates. In the later stage of the experiments with particularly thin substrates the trapped droplets were squeezed out of the contact area by a net force resulting from the pressure distribution within the contact region. Compared to the results of thick substrates with slow approach rates similar values for the effective friction coefficient were obtained.
Applying fast approaches to thick substrates leads to a mixed drainage scenario. The initial expulsion dynamics of an experimental run can be described in terms of an elastohydrodynamic behaviour however in the latter stages the layer expulsion exhibits dynamics similar to that seen for a slow ap-

proach.

5.4.2. Hexagonal shape of (n-1) islands

Apart from the measurements of the effective friction coefficient in the experiments with thick substrates described in the previous chapter, a close inspection of the snapshots of the expulsion of single liquid layers reveals more interesting details of the boundary line dynamics. The area with reduced film thickness n-1 is not always circular as predicted by theory, but instead shows edges and facets. Adjacent edges seem to cross at angles of approximately 60°, which is indicated by the white dashed lines in Figure 5.21. A more detailed analy-

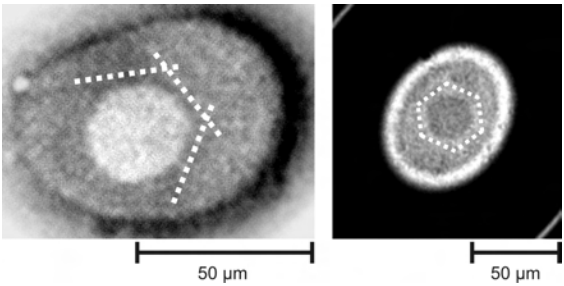

Figure 5.21: Shape of n-1 islands in different experiments. Both images show the transition $n = 3 \rightarrow 2$. The white dashed lines indicate the angle of 60°.

sis of this phenomenon is possible by extracting the boundary line from the transmission images. The orientation of short segments of the boundary along the circumference of the island can be extracted and analysed. The result is shown in the histogram in Figure 5.22. It is found that the facets

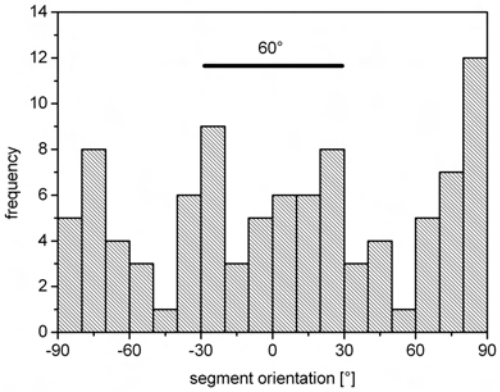

Figure 5.22: Histogram illustrating the orientation of short segments of the boundary. Note the preferred angle of approximately 60° between adjacent facets.

of the boundary line occur in orientations under a preferred angle of approximately 60° between adjacent facets. The origin of the hexagonally shaped dynamics of the expulsion process is an influence of the adjacent mica surface lattice, which shows a pseudo-hexagonal structure. Indeed, recent Monte Carlo simulations of OMCTS confined between mica surfaces showed that the liquid adopts the pseudo-hexagonal structure of the mica lattice [89, 90]. Similar effects were observed in experiments with liquid lead on a Si(100) surface, where the lead where the structure in the lead was affected by the Si surface [91, 92].
The observed effect was not reproducible in consecutive experiments. We therefore assume, that the effect is most likely very sensitive to the alignment of the surface lattice of the mica samples with respect to each other, which was not well-

controlled in the present experiments. With the light interferometry measurements it is not possible to investigate the in-plane layer structure in more detail. However, detailed investigations of the structure of the molecules within the single layers are possible with x-ray scattering experiments. In Chapter 6 experiments that combine both optical interferometry and x-ray scattering on thin liquid films in confinement will be presented.

6. In-plane layer structure of thin confined liquid films

As shown in the previous sections, confined liquid molecules arrange into layers parallel to the adjacent walls. The arrangement of the molecules affects the dynamics. Whether the thin liquid films solidify under confinement [11, 14, 87] or to what extent the dynamics are slowed down [12, 88] remains controversial issues. It was shown with the experiments presented in this work, that the single molecular layers are in a liquid-like state (at least during squeeze-out) and no confinement induced solidification was observed. However, a complete picture of the structure and the dynamics at the boundary between molecular motion and continuum flow has yet to emerge. In particular, the question of whether the structure of thin liquid confined layers changes from a liquid-like to a solid-like remains unanswered. More information about the in-plane layer structure can be obtained from x-ray scattering experiments.

X-ray diffraction experiments on confined liquids were first performed by C.R. Safinya *et al.* with an x-ray SFA [93, 94]. They report on the structure of thin smectic crystalline 8CB (4-cyano-4´-octylbiphenyl) films under confinement. 8CB molecules build dimers with overlapping cyanobiphenyl groups in the middle (Figure 6.1). These dimers order in a smectic-A-phase for temperatures below 33.5°C. Above 33.5°C

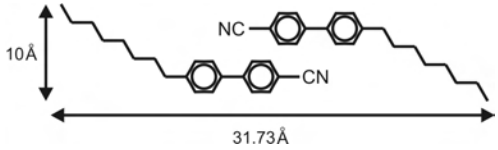

Figure 6.1: Chemical structure and dimensions of 4-cyano-4'-octylbiphenyl (8CB).

the liquid crystal undergoes a second order phase transition to the nematic phase (see e.g. [95] and references therein). Above 40.5°C 8CB forms an isotropic phase. The length of a dimer is 31.73 Å [96]. The so called director is along the long axis of the dimer. In thick confined 8CB films a flow induced layer orientation by shearing the confining walls can be measured by synchrotron x-ray scattering [96–98]. Furthermore it is known that the liquid crystals experience an orientation on solid surfaces [99]. Most common are the "homeotropic" orientation, where the director is perpendicular to the surface, and the "planar" orientation with the director parallel to the surface. This phenomenon is known as anchoring. On mica surfaces 8CB dimers orient typically in the planar configuration [99], due to polar interactions between the middle part of the 8CB dimer and the hydrophilic mica. The anchoring of 8CB on mica can be changed from parallel to homeotropic by making the surface hydrophobic using self-assembled monolayers [100]. As the mica surface lattice has a six-fold symmetry, it was observed that the orientation of the director adopts three different planar anchoring orientations at angles of 60° to each other [101, 102]. Making use of the optical birefringence of 8CB it was shown, that the dimers align most probably along the crystallographic β-axis of mica [66] (see Figure 6.2).
The first x-ray experiments on thin 8CB films in a SFA were

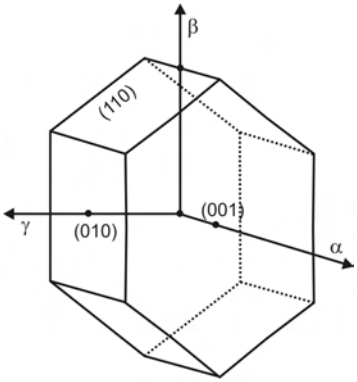

Figure 6.2: Schematic illustration to show the crystallographic axes of mica.

performed with an x-ray beam of ≈ 125 μm in diameter [93]. Over this relatively large width the thickness of the liquid profile changes owing to the curvature of the mica surfaces. Thus the x-ray scattering intensity is not measured at an exact film thickness but instead at an effective thickness that is an average of the film thickness across the beam width. In order to obtain improved measurements on thin liquid films in confinement we used modern x-ray techniques to perform experiments combining optical interferometry measurements with x-ray scattering using SFA2.

6.1. X-ray investigations on thin liquid crystalline 8CB films

Recent advances in synchrotron radiation sources and beam shaping techniques were used to measure the in-plane layer

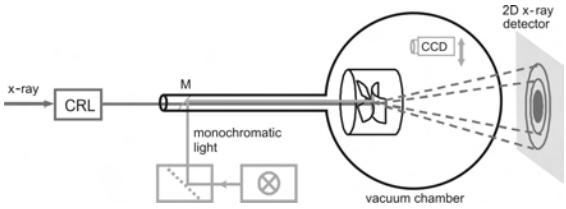

Figure 6.3: Schematic sketch of the set-up for experiments with combined optical and x-ray measurements. The SFA-cell is placed in a vacuum chamber in order to reduce air scattering. For optical measurements a rotatable mirror (M) couples the light into the SFA-cell and the CCD-camera records the transmission images. The x-ray ($E = 13.1$ keV) is micro-focused with a set of Compound Refractive Lenses (CRL)and fed through a vacuum tube.

structure depending on the film thickness. The optical SFA set-up was thus combined with x-ray measurements in experiments performed at the **E**uropean **S**ynchrotron **R**adiation **F**acility (ESRF) in Grenoble, France[1]. For this reason SFA2 was utilised as it fulfilled the different requirements of the x-ray experiments. Figure 6.3 displays a schematic sketch of the x-ray set-up. An x-ray beam with an energy of 13.1 keV was used, which was micro-focussed with a set of compound refractive lenses made of Beryllium[2]. With this technique it was possible to obtain a well focussed x-ray beam with a vertical beam size of 29.4 μm and a horizontal beam size of 19.3 μm at the sample position. A CCD-plate was used to record the scattering intensity in transmission through the sample geometry in the SFA. A small beam size at the sample position is of crucial importance, because otherwise one would

[1] The x-ray experiments (Si-1013) were performed at ID10A (Troïka).
[2] The CRL set used for the present experiment consisted of 29 lenses. Radius: 0.2 mm, radius of curvature: 0.447 mm, thickness: 0.01 mm.

obtain a scattering signal which is averaged over a large range of thickness of the liquid confined between the curved mica sheets. The very small scattering volumes investigated in these experiments result in small scattering intensities. Thus the signal to noise ratio must be increased as much as possible. This was achieved by placing the whole set-up into a vacuum vessel. In addition, the x-ray beam was fed through a vacuum pipe to reduce air-scattering. The experiments were performed at a pressure of a few 1e-3 mbar. In order to obtain a significant scattering signal of the liquid molecules the behaviour of confined liquid crystal 4-cyano-4 octylbiphenyl (8CB) was investigated. The scattering intensity arising from the smectic phase of the liquid crystal is much stronger that the one from OMCTS, which results in a higher signal to noise ratio especially for the thin films. Furthermore, the liquid crystal molecules interact strongly with the mica surface resulting in an anchoring effect of the molecules on the mica surface in preferred directions with respect to the surface lattice [99].
The experiments presented here were performed in the smectic-A-phase at temperatures of 23°C. In its ordered phases 8CB is birefringent. Bringing the surfaces into contact with the 8CB in between, one observes both continuous Newton fringes and such with small discontinuities (Figure 6.4). These discontinuities arise from differently oriented domains of a few microns in size. With decreasing distance from the contact area, the Newton fringes become suddenly continuous as a result of a confinement induced ordering of the liquid crystalline material. For the experiments combining optical interferometry with x-ray-scattering it is necessary to align the x-ray beam with respect to the contact area. This makes it possible to determine the degree of ordering and the orientation of the liquid crystal molecules depending on the film thickness. In the first set of experiments, scattering data from a confined 8CB film with thicknesses ranging from 3.9

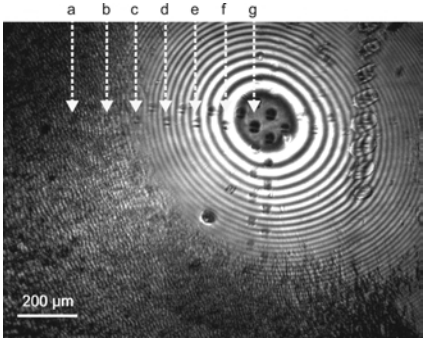

Figure 6.4: Transmission image of the mica samples in contact with liquid crystalline 8CB in between (taken after an x-ray measurement). The dark spots show the path of the x-ray measurements. In the region around the contact area the Newton fringes are continuous, which shows the confinement induced ordering of the birefringent 8CB molecules. At the edge of the image the fringes exhibit discontinuities. Here, the molecules arrange into micron-sized domains with different orientations. ($\lambda = 497.7$ nm).

μm to 8.4 nm were obtained (see Figure 6.5). The thickness of the liquid crystalline film was calculated from an optical image of the contact area (Figure 6.4 at the lateral positions denoted with a, b, ..., g). As expected, the total scattering intensity shows a linear dependence on the thickness of the confined 8CB film (Figure 6.6). A remarkable result of these experiments is that even for the thinnest 8CB film measured ($d_{8CB} = 8.4$ nm) a non-zero scattering intensity was obtained. The dark spots on Figure 6.4 indicate radiation damage of the silver layer. Optical microscopy images showed that the Ag layers dewetted from the mica surfaces due to the x-ray irradiation. While this affects the interferometry measurements, it may not have affected the x-ray measurements themselves. Therefore, we analyzed the 8CB-

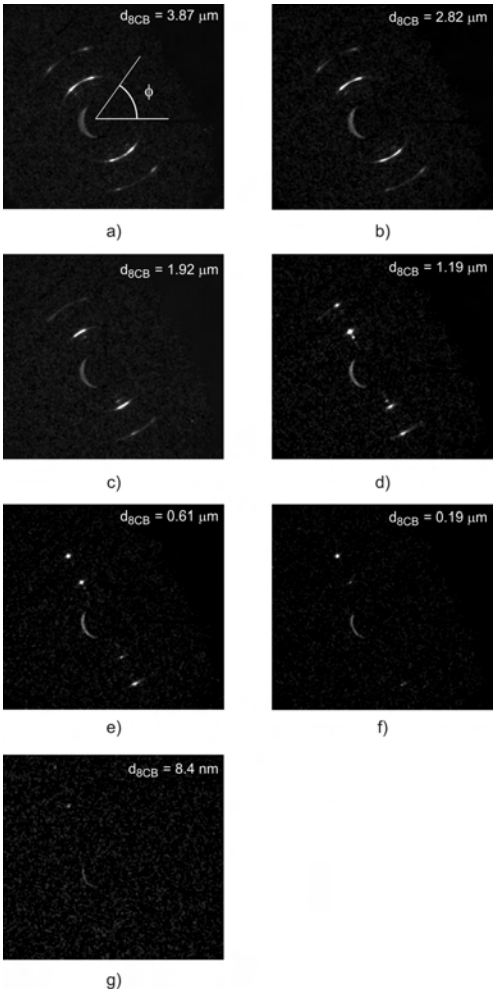

Figure 6.5: X-ray scattering images for different film thickness of 8CB. The measurements were taken at the positions with a, b, ..., g shown in Figure 6.4. Image size: (40×37) mm^2.

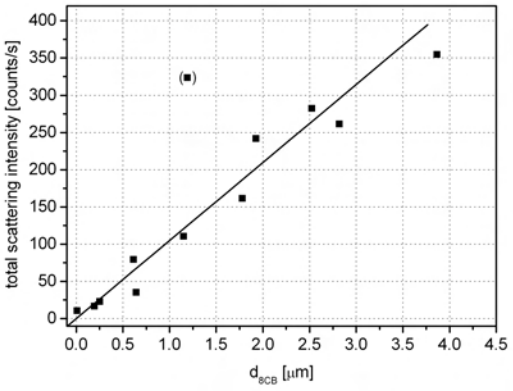

Figure 6.6: Linear dependence of the total scattering intensity on the thickness of the confined 8CB film.

facing mica surfaces on the opposite side of the damaged Ag layers using Atomic Force Microscopy (AFM) after rinsing off carefully the 8CB using ethanol: the AFM did not reveal any indication of surface damage. This supports the view that the 8CB film was not affected by the visible radiation damage in the Ag layers.
From the scattering images shown in Figure 6.5 one can obtain information about the ordering and the orientation of the confined 8CB molecules. Integrating the intensity along the radius vector (starting in the beam centre), the size of the molecules can be measured. The integrated intensity is plotted versus 2θ in Figure 6.7. 2θ is given by

$$\tan 2\theta = \frac{r}{L}, \tag{6.1}$$

where r is the radial distance from the beam-centre on the detector plate and L is the distance between sample and de-

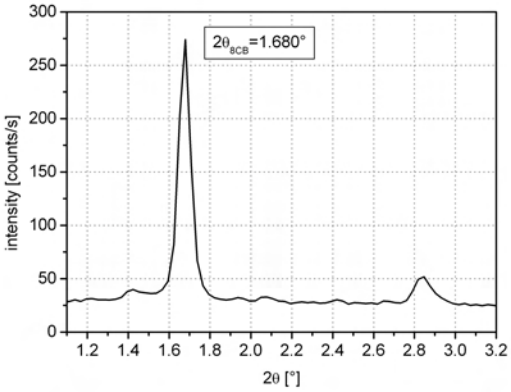

Figure 6.7: Azimuthal integration of the scattering intensity displayed on the image of Figure 6.5a). From the peak position one obtains for the length of the 8CB a value of 3.230 nm.

tector. Using simple geometrical calculations the dimension of the 8CB molecules can be determined from the peak of the radial intensity profile. Comparing the experimentally measured value of (3.230±0.113) nm for the length of the dimers, one finds a good agreement to the literature [96].
Another significant result of the x-ray experiments on confined liquid crystalline films is the following. Comparing the optical transmission image (Figure 6.4) and the scattering data (Figure 6.5) an interesting observation can be made. In the region of the disturbed Newton fringes the x-ray data show two distinct scattering peaks (Figure 6.5a) and b)) that arise from differently oriented domains of the liquid crystal. As the lateral distance to the contact area decreases, resulting in thinner 8CB films, the separation between these two peaks decreases (Figure 6.5c)). In the scattering images taken in

the region where the optical images shows undisturbed Newton fringes, only one scattering peak was detected (Figure 6.5d)-g)). Here, the liquid crystalline molecules arrange into one domain with a uniform orientation. This behaviour can be investigated in more detail by plotting the radially integrated intensity against the angle ϕ (Figure 6.8). This rep-

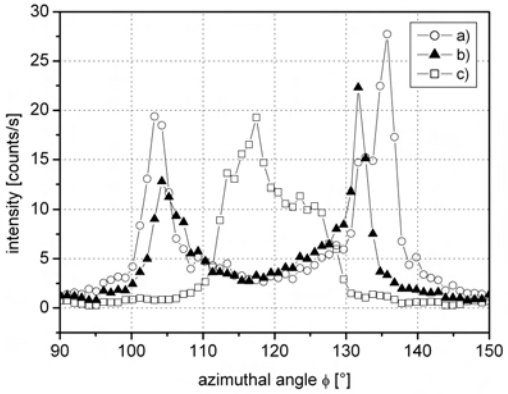

Figure 6.8: Plot of the radial integrated intensity versus azimuthal angle ϕ taken from the x-ray scattering images at the positions a)-c) in Figure 6.4. Two separated peaks were measured for $d_{8CB} = 3.87$ μm (a) and for $d_{8CB} = 2.82$ μm (b). In measurement (c) ($d_{8CB} = 1.92$ μm) the two peaks had already merged into one broader peak.

resentation of the scattering data reveals a further detail. Assuming that the 8CB dimers adopt only the orientations referring to the scattering peaks at $\phi_1 \approx 103°$ and $\phi_2 \approx 136°$, the intensity between the peaks should be zero (after subtracting the background). However, as can be seen in Figure 6.8, the intensity between the peaks is larger than beyond

the peaks. In this experiment, the top and the bottom sample were, by accident, not aligned parallel. The optical axes and thus the orientation of the surface lattice were determined after the x-ray experiment using polarised light and an analyser. The top and bottom sample were found to be horizontally rotated by an angle of $(35\pm5)^\circ$ with respect to each other. It was found from the optical measurements as well, that the angles ϕ_1 and ϕ_2 are compatible with the optical axes.
In order to describe this behaviour a simple model was assumed. The 8CB dimers close to the confining mica substrates orientate with the director parallel to the wall and with respect to the mica lattice [66,99,101,102]. In our model, the 8CB dimers adopt the orientation ϕ_1 and ϕ_2 induced by the adjacent mica surface lattice up to a certain thickness d_1 and d_2 respectively. The separation between the mica surfaces, i.e. the thickness of the liquid crystalline film is given by $d_{8CB} = d_1 + d_{1\to2} + d_2$. In the region between the molecules orientated with respect to the mica, the orientation is assumed to change linearly from ϕ_1 to ϕ_2. Each of these tran-

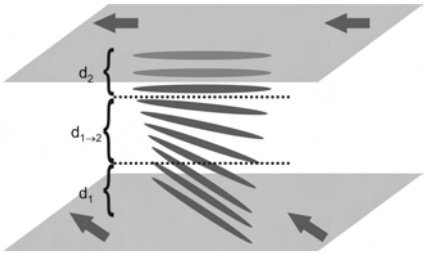

Figure 6.9: Schematic plot of the orientation of 8CB dimers with respect to the mica surface lattice in the region of disturbed Newton fringes. The mica samples induce the orientation of the dimers up to a certain separation from the surface. In the transition region $d_{1\to2}$ the 8CB dimers change their orientation linearly.

sition molecules contributes to the total scattering intensity which results in a non-zero value between the two main peaks at ϕ_1 and ϕ_2. Mathematically, we obtain a Gaussian distribution for the scattering intensity around ϕ_1 and ϕ_2 and a width of $\Delta\phi$ from the material oriented with respect to the mica surfaces:

$$I_i = d_i e^{-\frac{(\phi-\phi_1)^2}{2(\Delta\phi)^2}} \quad \text{with} \quad i = 1, 2. \tag{6.2}$$

The dimers in the transition regime change the orientation linearly from ϕ_1 to ϕ_2 and each dimer contributes to the scattering intensity between the peaks at ϕ_1 and ϕ_2. This is described with:

$$I_{1\to 2} = \sqrt{\frac{\pi}{2}}\Delta\phi \left[\text{erf}\left(\frac{\phi-\phi_1}{\sqrt{2}\Delta\phi}\right) - \text{erf}\left(\frac{\phi-\phi_2}{\sqrt{2}\Delta\phi}\right)\right] \tag{6.3}$$

The total scattering intensity is then obtained from the sum of I_1, I_2 and $I_{1\to 2}$.
Comparing the experimental data with this model, best fit values for the thickness of the regimes with different orientations were found. Figure 6.10 shows the experimental data and the fitting curve.

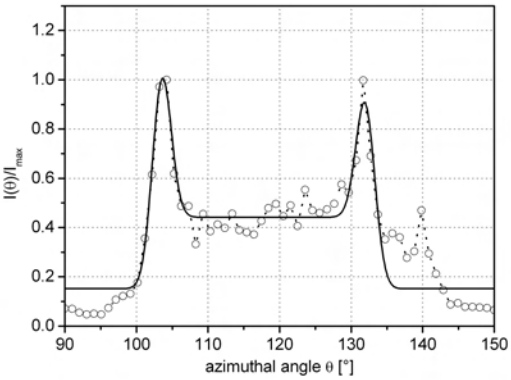

Figure 6.10: Experimental profile of the intensity versus azimuthal angle (open circles) compared with the fitting curve of the assumed model. The peaks at $\phi_1 = 103.4°$ and $\phi_2 = 132.1°$ arise from lattice induced orientation of the 8CB molecules. This orientation extends to 18.4% of the total thickness of the 8CB film ($d_{8CB} = 2.57$ μm) for orientation ϕ_1 and to 15.8% for ϕ_2. 65.8% of d_{8CB} belong to the transition region $d_{1\to 2}$ and contribute to the scattering intensity between the main peaks.

Assuming the model describes the situation correctly, for this 8CB thickness approximately 66% of the total film thickness (i.e. 1.69 μm) are in the transition region. The orientations ϕ_1 and ϕ_2 are in good agreement with the measured orientation of the substrates. Performing the fitting to a thicker 8CB film such as in Figure 6.5a)($d_{8CB} = 3.87$ μm) we find that 29% of the the total film thickness (i.e. 1.12 μm) are in the transition region. As already mentioned above, for decreasing film thicknesses the two peaks merge into one single scattering peak. It is interesting to note that the two differ-

ent domains merge into one at a film thickness (of approx. 2 μm) that corresponds to the thickness of the twisted transition region $d_{1\rightarrow 2}$. It is remarkable that here the orientation adopts a value between ϕ_1 and ϕ_2. It thus appears that the confinement induced ordering is stronger than the anchoring effects to one of the orientations induced by the substrates.
An alternative interpretation of the scattering data shown in Figure 6.5 is as follows. In the regime of the disturbed Newton fringes the liquid crystal arranges into many domains with different orientations. With the present parameters of the x-ray beam it is conceivable, that we obtain the scattering intensity laterally averaged over two domains with different orientations. However, with the present experimental results it is not possible to decide, which interpretation describes the behaviour of the liquid crystal correctly.
On the basis of these results, obtained by combining light interferometry and x-ray scattering in a SFA geometry, a more detailed investigation of this behaviour will be done in future experiments. In particular, studies of the influence of the substrate misalignment as well as temperature-dependent measurements are planned for the future. In addition, the extent to which the phase transitions of the liquid crystal are influenced by the confinement will be investigated.

7. Conclusion

Conclusions have been drawn in the various sections of this thesis at the appropriate points. This chapter now summarises those conclusions and suggests possible future work to extend the results.

7.1. Summary

The set-up and measurement procedures for the two-dimensional imaging SFA have been described in significant detail owing to the originality of this new experimental technique. The central feature of the instrumentation developed are two SFA cells (SFA1 and SFA2) each created with specific properties relating to the requirements of the experiments being performed. SFA1 was constructed exclusively to allow optical measurements of the collapsing dynamics of single liquid layers. With its small chamber volume, enabling the x-ray scattering signal to noise ratio to be optimised, SFA2 made experimental investigations of the in-plane structure of molecularly thin lubricant layers possible.
The problem of erroneous surface force measurements arising from nanoparticulate contamination of mica surfaces was recognised and a re-cleaving technique was developed to avoid this issue. The re-cleavage of mica substrates immediately prior to the experiment has been described in detail and demonstrated to be a successful procedure for avoiding sur-

face contamination with nanoparticles. This step is of crucial importance for all of the results obtained.
Using the unique two-dimensional capability of the SFA constructed during the course of the work presented here, the dynamics of drainage of molecularly thin films has been investigated. This spatially resolved imaging technique has allowed for a detailed analysis of hydrodynamic processes in liquid films of nanoscopic thickness. Unprecedented insights into the stability and the collapse dynamics of liquid films with a discrete layer structure have been obtained. In particular, it has been shown that the collapse dynamics of lubricant layers in this thickness range depends critically on the elasticity of the substrates and the applied load ramps.
For thick and thin mica substrates with low approach rates the dynamics of the roughly circular boundary line can be described analytically by the Persson-Tosatti model when the nucleation of the reduced film thickness takes place in the centre of the contact area. If the nucleation happens far away from the centre of the contact area, the boundary line assumes a characteristic double S-shape [6]. In this case, a quantitative description can only be obtained numerically [57]. If the mica sheets are particularly thin, the boundary line may become unstable and roughen during the growth phase [58]. This can even lead to the formation of trapped pockets of liquid left behind in the contact area in the final stage of the collapse. When particular thin mica sheets are approached at high rates, elastohydrodynamic deformation of these soft substrates leads to simultaneous nucleation of the layer collapse at several positions along the rim of the contact area [48]. For high approach rates on thick substrates a mixed scenario can be observed. Initially the dynamics can be described in terms of an elastohydrodynamic behaviour however in the latter stages the layer expulsion exhibits dynamics similar to that seen for a slow approach.
For a specific model lubricant, namely that of OMCTS, the

thickness dependence of the effective viscosity has been determined. The sensitivity of the two-dimensional imaging technique in terms of effective viscosity is about two orders of magnitude better than the highest reported resolution in shear force measurements [11]. It was found that the effective viscosity increases by approximately one order of magnitude upon decreasing the film thickness from six to two layers. This result is remarkable, because it is in contrast to earlier results that reported an increase in the viscosity by several orders of magnitude within roughly the same range of film thickness [11, 12]. In [11, 12] the possibility that the substrates were contaminated with nanoparticles seems likely as traditional preparation techniques were used. In more recent experiments by others [71–73], where contamination free surfaces are assured, this increase in the effective viscosity by several orders of magnitude is not reproducible.

In order to explain the increase in effective viscosity with decreasing film thickness the hydrodynamic model is extended to include two different friction coefficients; a liquid-solid friction coefficient taking into account the interaction between a liquid layer and a solid wall, and a liquid-liquid friction coefficient arising from the sliding of two adjacent liquid layers on top of each other. The model is found to be consistent with the experimental data and the origin of the increase of the effective viscosity with decreasing film thickness is attributed to the increasing weight of the liquid-solid coefficient with decreasing film thickness.

A closer inspection of the two-dimensional imaging SFA experiments on thick substrates revealed that the area with reduced film thickness is not circular as predicted by theory but instead shows edges and facets. A more detailed investigation of the structure of the molecules within single layers is made by combining optical interferometry with x-ray scattering experiments. As expected, the scattering intensity decreased linearly with decreasing thickness of the confined

liquid crystalline film. Remarkably, even for very thin 8CB films (d_{8CB} = 8.4 nm) a non-zero scattering intensity was obtainable. The layer spacing of the 8CB molecules was measured and found to be in good agreement with the literature. Furthermore the orientation of the liquid crystal with respect to the surface lattice of the mica was investigated. For thick films of 8CB two different orientations of the dimers, according to the orientation of the mica lattice, were found. The separation between the two scattering peaks (corresponding to the two orientations) decreased for decreasing film thickness. The peaks merged at an 8CB thickness, where in the optical image the Newton fringes became continuous. In the regime of the undisturbed fringes the dimers adopt an orientation between the angles expected from the anchoring to the substrates. Thus, the confinement induced orientation seems to be stronger than the anchoring effect. A simple model was presented that describes the experimental observation of a non-zero scattering intensity between the two peaks at large film thicknesses in terms of three regimes with different dimer orientations.

7.2. Future work

The set-up of our two-dimensional imaging SFA allows detailed investigations of the expulsion dynamics of thin liquid films under confinement. This is a powerful experimental tool and the investigation of the dynamics of expulsion processes should now be broadened. For instance, different lubricants and in particular liquids with more complicated molecules should be studied. Factors such as the effect of temperature on the dynamics of expulsion processes are also open to exploration. Modifications of the surface chemistry, such as wettability patterned substrates, on the dynamics of

drainage processes should also provide a fruitful area of further experiments. Currently, the two-dimensional imaging SFA is being adapted to allow the observation of diffusion of the molecules in the confined geometry. This is achieved simply by incorporating a laser into the SFA set-up thus allowing FRAP (Fluorescence Recovery After Photobleaching) measurements to be performed.
Preparations are underway for future experiments using the combined x-ray and optical interferometry technique described in Section 6.1. First, the influence of the substrate orientations on the in-plane ordering of the confined liquid will be investigated. Secondly, it is planned to study to what extent the phase transitions in 8CB are affected by confinement. Finally, shear induced ordering of the liquid crystal film will be examined.

A. Appendix A

The following table details the core components (instrumentation and chemicals) of the experimental set-up.

Table A.1: List of components and chemicals

Device	**Specifications/model**	**Manufacturer**
SFA1	custom-designed (dynamical measurements)	Workshop University of Ulm
SFA2	custom-designed (x-ray experiments)	Workshop University of Ulm
Piezo tube	L=2.5", OD=0.5"	Staveley Sensors
Piezo motor	PicoMotor 8322	New Focus
Sample support	Radii of curvature: R=5 cm and R=7 cm	Workshop University of Ulm
Microscope cover slides	(12×19.5) mm, thickness 00 (60...80 μm), type: Q1520	PLANO GmbH (Wetzlar)
Cylinder lenses	quartz glass, radius of curvature R=2 cm (custom designed)	Hellma Optik GmbH (Jena)

Device	Specifications/model	Manufacturer
Power supply	model: E3648A (remote controlled)	Agilent Technologies
HV amplifier	T-401 basic amplifier module (incl. inverting and gain selector)	ElbaTech
Permanent magnets	NdFeB, type: NE44	IBS Magnet (Berlin)
Xe-arc lamp	XBO 300W, power supply SVX1530 with lamp case LAX	Müller Elektronik Optik GmbH
Hg(Ar) calibration lamp	model LSPO35	LOT Oriel
Monochromator	1/8m grating Monochromator, grating: 1200 lines per mm, model: 77200	LOT Oriel
CCD camera	1380 x 1024 pixel, 10 fps at maximum resolution, 20 fps at 2x-Binning mode, model: Pixefly Standard HiRes 220XS	PCO Optics
5x Objective	NA=0.13, WD 22.5 mm	Nikon
20x Objective	NA=0.35, WD 20.5 mm	Nikon
Heat exchanger	model: WT2000010	Tiger Electronics
Thermostat	heating power: 2.25 kW, cooling power (20°C): 0.2 kW, model: RE306 Ecoline	LAUDA

Device	Specifications/model	Manufacturer
Mica	Muscovite ruby mica sheets, high quality	B&M Mica Co., Inc. (USA)
Glue	Epon Resin1004F	Shell Chemical Co.
OMCTS	Octamethylcyclo-tetrasiloxane, purity: 99%	Sigma Aldrich
8CB	4-cyano-4´-octyl-biphenyl, purity: 98%	Sigma Aldrich

Bibliography

[1] B.N.J. Persson. Sliding friction - physical principles and applications. *Springer Verlag Berlin*, 2000.

[2] B.N.J Persson and E. Tosatti. *Phys. Rev. B*, 50(8):5590–5599, 1994.

[3] J.N. Israelachvili. Intermolecular and surface forces. *Academic Press London*, 1991.

[4] D.Y.C. Chan and R.G. Horn. *J. Chem. Phys.*, 83(10):5311–5324, 1985.

[5] H.K. Christenson. *J. Chem. Phys.*, 78(11):6906–6913, 1983.

[6] F. Mugele and M. Salmeron. *Phys. Rev. Lett.*, 84(25):5796, 2000.

[7] F. Mugele, T. Becker, A. Klingner, and M. Salmeron. *Coll. Surf. A: Physicochemical and Engineering Aspects*, 206:105–113, 2002.

[8] R.G. Horn and J.N. Israelachvili. *J. Chem. Phys.*, 75(3):1400–1412, 1981.

[9] M. Heuberger, M. Zäch, and N. D. Spencer. *Science*, 292(5518):905–8, 2001.

[10] T. Becker and F. Mugele. *Phys. Rev. Lett.*, 91(16):166104–1–4, 2003.

[11] J. Klein and E. Kumacheva. *Science*, 269:816–819, 1995.

[12] A.L. Demirel and S. Granick. *Phys. Rev. Lett.*, 77(11):2261–4, 1996.

[13] J.N. Israelachvili, P.M. McGuiggan, and A.M. Homola. *Science*, 240:189, 1988.

[14] J. Klein and E. Kumacheva. *J. Chem. Phys.*, 108(16):6996–7009, 1998.

[15] A.L. Demirel and S. Granick. *J. Chem. Phys.*, 115(3):1498–1512, 2001.

[16] B.N.J Persson and P. Ballone. *J. Chem. Phys.*, 112(21):9524–9542, 2000.

[17] B.N.J Persson and F. Mugele. *J. Phys.: Cond. Matt.*, 16:R295–R355, 2004.

[18] B.N.J Persson. *Chem. Phys. Lett.*, 324:231–239, 2000.

[19] T. Becker and F. Mugele. *J. Phys.: Cond. Matt.*, 15:321–330, 2003.

[20] A. Dhinojwala. *Mat. Sci. Tech.*, 19:1170–1174, 2003.

[21] B.V. Derjaguin and L. Landau. *Acta Physicochim. URSS*, 14:633–662, 1941.

[22] E.J.W. Verwey and J.T.G. Overbeek. Theory of stability of lyophobic colloids. *Elsevier (Amsterdam)*, 1948.

[23] R.M. Pashley and J. Israelachvili. *Colloid Interface Sci.*, 101:511, 1984.

[24] W. v.Megen and I.K. Snook. *J. Chem. Soc. Faraday Trans. II*, 75:1095, 1979.

[25] F.F. Abraham. *J. Chem. Phys.*, 68:3713–3716, 1978.

[26] M. Rao, B.J. Percus, and M.H. Kalos. *J. Chem. Phys.*, 71:3802–3806, 1979.

[27] R. Evans and A.O. Parry. *J. Phys. Cond. Matt.*, 2:SA15–SA32, 1990.

[28] F. Kremer, A. Huwe, M. Arndt, P. Behrens, and W. Schwieger. *J. Phys.:Cond. Matt.*, 11:A175–A188, 1999.

[29] E. Kossel, M. Weber, and R. Kimmich. *Sol. State Nucl. Magn. Res.*, 25:28–34, 2004.

[30] I. Ardelan, G. Farrher, C. Mattea, and R. Kimmich. *J. Chem. Phys.*, 120:9809–9816, 2004.

[31] J.N. Israelachvili and D. Gourdon. *Science*, 292(5518):867–868, 2001.

[32] V.S.J. Craig, C. Neto, and D.R.M. Williams. *Phys. Rev. Lett.*, 87(5):054504–1–4, 2001.

[33] H.K. Christenson. *Chem. Phys. Lett.*, 118(5):455–458, 1985.

[34] S. Loi, G. Sun, V. Franz, and H.J. Butt. *Phys. Rev. E*, 66:031602, 2002.

[35] D. Tabor and R.H.S. Winterton. *P. Roy. Soc. Lond. A Mat.*, 312:435, 1969.

[36] J.N. Israelachvili and D. Tabor. *P. Phys. Soc. Lond. A*, 331:19, 1972.

[37] P.K. Hansma, V.B. Elings, O. Marti, and C.E. Bracker. *Science*, 242:209–216, 1988.

[38] W.F. Heinz and J.H. Hoh. *Nanotechnology*, 17:143, 1999.

[39] D. Sarid. *Oxford University Press*, 1994.

[40] G. Sun, E. Bonnaccurso, V. Franz, and H.J. Butt. *J. Chem. Phys.*, 117(22).

[41] S.J. O'Shea, M.E. Welland, and T. Rayment. *Appl. Phys. Lett.*, 60:2356–2358, 1992.

[42] S.J. O'Shea and M.E. Welland. *Langmuir*, 14:4186–4197, 1998.

[43] Y. Zhu and S. Granick. *Phys. Rev. Lett.*, 87(9), 2001.

[44] H.J. Butt and V. Franz. *Phys. Rev. E*, 66:031601, 2002.

[45] V. Franz and H.J. Butt. *J. Phys. Chem. B*, 106:1703, 2002.

[46] C. Cottin-Bizonne, S. Jurine, J. Baudry, J. Crassous, F. Restago, and É. Charlaix. *Eur. Phys. J. E*, 9:47–53, 2002.

[47] P. Martin, P. Silberzan, and F. Brochard-Wyart. *Langmuir*, 13:4910–4914, 1997.

[48] P. Martin and F. Brochard-Wyart. *Phys. Rev. Lett.*, 80(15).

[49] H.K. Christenson and C.E. Blom. *J. Chem. Phys.*, 86(1):419–423, 1987.

[50] H.K. Christenson. *J. Phys. Chem.*, 97(46):12034–12041, 1993.

[51] J.G. Dash. Films on solid surfaces. *Academic, New York*, 1975.

[52] P.G. deGennes. *Rev. of Mod. Phys.*, 57(3):827–863, 1985.

[53] W. Zisman. in "contact angle, wettability and adhesion". *ed. by F.M. Fowkes, Advances in Chemical Series No. 43 (Am. Chem. Soc., Washington, DC, 1964).*

[54] E. Brener. *Phys. Rev. Lett.*, 71:3653, 1993.

[55] J.S. Langer. *Phys. Rev. A*, 36:3350, 1987.

[56] S. Zilberman, B.N.J. Persson, and A. Nitzan. *J. Chem. Phys.*, 115(24):11268–77, 2001.

[57] S. Zilberman, T. Becker, F. Mugele, B.N.J. Persson, and A. Nitzan. *J. Chem. Phys*, 118(24):11160–11167, 2003.

[58] S. Zilberman, B. N. J. Persson, A. Nitzan, F. Mugele, and M. Salmeron. *Phys. Rev. E*, 63(5):055103/1–4, 2001.

[59] J.N. Israelachvili and G.E. Adams. *J. Chem. Soc. Farad. Trans.*, 1(74):975, 1978.

[60] M. Heuberger, G. Luengo, and J. Israelachvili. *Langmuir*, 13:3839–3848, 1997.

[61] M. Born and E. Wolf. Principles of optics. *Cambridge University Press*, 6th ed., 1999.

[62] E. Hecht. Optics. *Addison Wesley Longman, Inc.*, 3rd ed., 1998.

[63] P.B. Johnson and R.W. Christy. *Phys. Rev. B*, 6(12):4370–4379, 1972.

[64] R.E. Kirk, D.F. Othmer, and M. Grayson. *New York (Wiley)*, 16(4ed.), 1991.

[65] University of New Brunswick (Canada) Dept. of Geology. Lecture 26: Micas. *http://www.unb.ca/courses/geol/2142/LEC-26.html.*

[66] A. Artsyukhovich, L.D. Broekman, and M. Salmeron. *Langmuir*, 15(6):2217–2223, 1999.

[67] A.I. Bailey and S.M. Kay. *Brit. J. Appl. Phys.*, 16:39–44, 1965.

[68] P. Frantz and M. Salmeron. *Trib. Lett.*, 5(2-3):151–153, 1998.

[69] S. Ohnishi, M. Hato, K. Zamada, and H.K. Christenson. *Langmuir*, 15:3312–3316, 1999.

[70] F. Mugele, B.N.J Persson, S. Zilberman, A. Nitzan, and M. Salmeron. *Tribol. Lett.*, 12(2):123–129, 2002.

[71] M. Heuberger and M. Zäch. *Langmuir*, 19:1943–1947, 2003.

[72] J.N. Israelachvili, N.A. Alcantar, N. Maeda, T.E. Mates, and Marina Ruths. *Langmuir*, 20:3616–3622, 2004.

[73] Y. Zhu and S. Granick. *Langmuir*, 19:8148–8151, 2003.

[74] Roger G. Horn and Douglas T. Smith. *Appl. Opt.*, 30(1):59–65, 1991.

[75] M. Heuberger. *Rev. Sci. Instr.*, 72(3):1700–1707, 2001.

[76] M. Zäch. PhD thesis, ETH Zürich, 2002.

[77] J.N. Israelachvili. *J. Coll. Int. Sci.*, 44(2):259–272, 1973.

[78] V.S. Mangipudi. *J. Coll. Int. Sci*, 175:484–491, 1995.

[79] B.N.J Persson, V.N. Samoilov, S. Zilberman, and A. Nitzan. *J. Chem. Phys.*, 117(8):3897–3914, 2002.

[80] F. Brochard and P.G. de Gennes. *Langmuir*, 8:3033–3037, 1992.

[81] P.A. Thompson and M.O. Robbins. *Phys. Rev. A*, 41(12):6830–6837, 1990.

[82] L. Pozhar. *Phys. Rev. E*, 61(2):1432–1446, 2000.

[83] R. Seemann, S. Herminghaus, and K. Jacobs. *Phys. Rev. Lett.*, 87(19):196101–1–4, 2001.

[84] S.P. Timoshenko and J.N. Goodier. *McGraw-Hill, New York*, 1987. Chapter 12, page 138.

[85] K.L. Johnson, K. Kendal, and A.D. Roberts. *Proc. R. Soc. London, Ser. A*, 324:301–313, 1971.

[86] R.G. Horn, J.N. Israelachvili, and F. Pribac. *J. Coll. Int. Sci.*, 115(2):480–492, 1987.

[87] E. Kumacheva and J. Klein. *J. Chem. Phys.*, 108:7010, 1998.

[88] A. Mukhopadhyay, J. Zhao, S.C. Bae, and S. Granick. *Phys. Rev. Lett.*, 89(13):136103–1–4, 2002.

[89] J.E. Curry. *J. Chem. Phys.*, 113(6):2400–2406, 2000.

[90] J.E Curry. *Mol. Phys.*, 99(9):745–752, 2001.

[91] H. Reichert, O. Klein, H. Dosch, M. Denk, V. Honkimäki, T. Lippmann, and G. Reiter. *Nature*, 408:839–841, 2000.

[92] H. Reichert. *Physik J.*, 7/8:83, 2002.

[93] S.H.J. Idziak, C.R. Safinya, R.S. Hill, K.E. Kraiser, M. Ruths, H.E. Warriner, S. Steinberg, K.S. Liang, and J.N. Israelachvili. *Science*, 264:1915–1918, 1994.

[94] S.H.J. Idziak, I. Koltover, J.N. Israelachvili, and C.R. Safinya. *Phys. Rev. Lett.*, 76(9):1477–1480, 1996.

[95] M. Ruths, S. Steinberg, and J.N. Israelachvili. *Langmuir*, 12:6637–6650, 1996.

[96] C.R. Safinya, E.B. Sirota, R.F. Bruinsma, C. Jeppesen, R.J. Plano, and L.J. Wenzel. *Science*, 261:588–591, 1993.

[97] C.R. Safinya, E.B. Sirota, R. Plano, and R.F. Bruinsma. *J. Phys.: Cond. Matt.*, 2:SA365–SA371, 1990.

[98] C.R. Safinya, E.B. Sirota, and R.J. Plano. *Phys. Rev. Lett.*, 66(15):1986–1989, 1991.

[99] P. Pieranski and B. Jerome. *Phys. Rev. A*, 40(1):317–322, 1989.

[100] J. Janik, R. Tadmor, and J. Klein. *Langmuir*, 13:4466–4473, 1997.

[101] L.M. Blinov and A.A. Sonin. *Mol. Cryst. Liq. Cryst.*, 179:13, 1990.

[102] J. Bechhoefer, B. Jerome, and P. Pieranski. *Phase Trans.*, 33:227, 1991.

List of own Publications

Parts of this thesis have been or will be published in the following articles:

T. Becker and F. Mugele:
"Nanofluidics: Molecularly thin lubricant layers under confinement", *Molecular Simulation* (accepted)

T. Becker and F. Mugele:
"Mechanical properties of molecularly thin lubricant layers: Experimental methods and procedures", *J. Phys.: Cond. Matt.***17**(9), p. S319-S332 (2005)

T. Becker and F. Mugele:
"Nanofluidics: Viscous dissipation in layered liquid films", *Phys. Rev. Lett.* **91**(16), p. 166104-1-4 (2003)

T. Becker, F. Mugele:
"Collapse of molecularly thin lubricant layers between elastic substrates", *J. Phys.: Cond. Matt.* **15**, p. S321-S330 (2003)

S. Zilberman, T. Becker, F. Mugele, B.N.J. Persson, and A. Nitzan:
"Dynamics of squeeze-out: Theory and experiments", *J. Chem. Phys.* **118**(24), p. 11160-11167 (2002)

F. Mugele, T. Becker, A. Klingner, and M. Salmeron: "Two-dimensional observation of drainage and layering transitions in confined liquids", *Coll. Surf. A* **206**, p. 105-113 (2002)

Acknowledgement

First of all I would like to thank my supervisor Prof. Dr. Frieder Mugele, who offered me the opportunity of doing my PhD in his group in the field of confined thin liquid films. Since the beginning of this work, Frieder has set high expectations and I value the positive effect this has had on me. It was not always easy for me to answer all his questions, but they motivated me to go on and on. He also gave me the possibility to present my results on several conferences all over the world. I also remember some nice evenings after work, where we went out for sports and drinks. I appreciated very much working with Frieder and I wouldn't hesitate to ask him again for a PhD position.
I also wish to acknowledge the guidance and support of Prof. Dr. Stephan Herminghaus, the head of the Applied Physics department of the University in Ulm.
Further I want to thank Prof. Dr. W.J. Briels and Prof. Dr. D.H.A. Blank from the University of Twente for joining my PhD committee.
Without the help of our technician Udo Krafft, I would have been lost many times. He always found solutions for the changes I wanted to include to the set-up. Additionally I'd like to say thank you to the staff of the workshop at the University of Ulm for manufacturing many parts of the set-up.
Meeting Dr. Harald Reichert from the Max Planck Institute für Metallforschung in Stuttgart enabled me to perform

the x-ray experiments at the ESRF in Grenoble. His enthusiasm for the x-ray scattering investigations with the SFA made the stays in France very pleasant and successful. I also thank Dr. Cristian Mucota, Veijo Honkimäki, Federico Zontone, Anders Madsen and Thomas Buslaps for technical assistance in Grenoble. I am grateful for the contributions of Bo Persson and Silviu Zilberman to the theory and numerical simulations.
I had a great time in the department of Applied Physics in Ulm and I want to thank all members of the department for the discussions and the very nice atmosphere. A special thanks goes to Tamara, Manuela, Helmut and Benjamin. You'll now keep alive the spirit of our group in Twente.
I'm very happy, that I met Daniel, Alex and Lothar during my studies in Ulm. Thank you for the great time we spent together and for being very good friends.
I also want to express my gratitude to Bernie, Reinhard, Lobby and Ralf for being the best friends ever.
All my studies and this thesis would not have been possible without the help of my family. Thank you Mum and Dad, Andi and Fee, Oma and Opa and Ingrid for all your support over the years.
Finally I want to thank Nicole. Without you, this work would not have reached this stage. Thank you for all your help and motivation. In all the time you made the sun shine in my mind with your love.